Lyman Break Galaxies at $z \sim 5$: Luminosity Function

Ikuru Iwata

Department of Astronomy, Faculty of Science,
Kyoto University, Japan 606–8502

22 Jan. 2003

Contents

Chapter 1

Introduction

1.1 The Lyman Break Method and LBGs at z $\sim$ 3–4

In the past several years, observational studies of galaxy formation and evolution have been remarkably progressed, thanks to the improvement of the observational methods and, in particular, the development of 8 to 10m-class telescopes and space-based facilities such as the Hubble Space Telescope (HST).

One of the most important progresses is that statistical nature of high redshift galaxies has been revealed through a finding of many normal (non-AGN) galaxies at high redshift universe, which has been enabled by the Lyman break method pioneered by Steidel and his collaborators (e.g., [Steidel and Hamilton 1992]; [Steidel et al. 1996a]). Basically, it aims to detect the "break" in the spectral energy distribution (SED) at around the Lyman limit (912 Å) due to the intervening neutral hydrogen, by the deep broad-band imaging in multiple wavebands. Because the method only requires the broad-band imaging, the telescope time needed to construct a sample is much smaller than that for a spectroscopic survey. Also, contrary to the narrow-band imaging survey, which intends to detect a specific emission line at a limited range of redshift, the Lyman break method can detect objects at relatively wider redshift range, so at a same limiting magnitude the number of a sample detected by the Lyman break method can be larger than that detected by the narrow-band imaging survey, and it allows researchers to discuss the properties of the galaxies at high redshift with smaller statistical errors.

Since their first discovery in early 1990s, the Lyman break galaxies (LBGs) at $z \sim 3$–4 have been extensively investigated in various ways and knowledge on their nature has been accumulated. Here we briefly summarize the results of the past studies on LBG.

1.1.1 Imaging Surveys and Optical Spectroscopy

Initially the broad-band imaging survey for galaxies at high redshift was targeted to the fields around the high redshift quasars, followed by the surveys of general (blank) fields. Steidel et al. ([Steidel and Hamilton 1992]; [Steidel and Hamilton 1993]; [Steidel et al. 1995]) made a search for LBGs at $z \sim 3$ using CTIO 4m telescope. They use custom-made U_n, G, $\mathscr{R}$-band filters optimized for the detection of galaxies at $z \sim 3$.

[Steidel et al. 1996a] made a follow-up optical spectroscopy of LBG candidates, using the Keck telescope. Among the 23 objects identified, 16 (70.0%) objects are identified as galaxies at $z \sim 3$ and three are identified as QSOs. Their rest-frame UV spectra resemble those of nearby active star-forming galaxies; they have flat UV continua and strong high-ionization stellar lines, often showing P-cygni profiles. The star formation rates estimated from (dust-uncorrected) UV luminosity ranges 4–25 h_{50}^{-2} $M_\odot$ yr^{-1}, with a typical value of 8.5 h_{50}^{-2} $M_\odot$ yr^{-1}. [Steidel et al. 1996b] also report a spectroscopic confirmation of LBGs in the Hubble Deep Field-North (HDF-N; [Williams et al. 1996]). The target objects showed a spectral discontinuity between F300W and F450W passbands. Among 8 galaxies observed with the Keck telescope with LRIS, three objects are contaminated by nearby stars and galaxies. Except for them, redshifts of all five galaxies are confirmed to be between 2.59 and 3.22. To date more than 500 LBGs at $z \sim 3$ have been spectroscopically identified, mainly by LRIS on the Keck telescopes (e.g., Giavalisco(1996); Cohen(2000); Adelberger(2003)).

[Giavalisco et al. 1996] report the results of HST/WFPC2 imaging observations for spectroscopically confirmed LBGs at $z > 3$. They have compact cores which typically contain 90–95% of total luminosity of the galaxies and have a few kpc in half light radius. The cores are often surrounded by more extended, lower surface brightness component. The radial profiles of the galaxies are well fitted by $r^{1/4}$ law or exponential profiles. They note that LBGs often show spherically symmetric profiles, in contrast to the elongated or disrupted appearances found for galaxies at $z \sim 1$.

The clear signal of spatial clustering of the LBGs at $z \sim 3$ has been reported (e.g., [Steidel et al. 1998]; [Giavalisco et al. 1998]), and the comparison with the models of cold dark matter (CDM) halos suggests that their clustering properties of the LBGs can be ascribed to the biased galaxy formation [Giavalisco and Dickinson 2001].

[Steidel et al. 1999] extend their ground-based LBG search to $z \sim 4$. They surveyed a 828 arcmin^2 area in total which is comprised of 10 fields and found 244 galaxies with $I_{\rm AB} \leq 25.0$ mag. The luminosity function of the LBGs at $z \sim 4$ remarkably resembles that at $z \sim 3$, indicating that no significant evolution of luminosity function occurs from $z = 4$ to $z = 3$ (about 0.6 Gyr for the cosmology with $\Omega_{\rm M} = 0.3$, $\Omega_\Lambda = 0.7$ and $H_0 = 65$ km s^{-1} Mpc^{-1}). [Ouchi et al. 2001a] also report the result of their own LBG survey for $z \sim 4$ in the field of *SUBARU/XMM* Deep Survey. They found that the luminosity function almost agrees with that obtained by [Steidel et al. 1999] and that the significant clustering is seen.

1.1.2 Near-infrared Imaging and Spectroscopy

Their stellar population has been investigated by comparing the optical to near-infrared spectral energy distributions (SEDs) with stellar population synthesis models ([Sawicki and Yee(1998]; [Papovich et al. 2001]; [Shapley et al. 2001]). [Shapley et al. 2001] used rest-frame UV-to-optical (900 – 5500 Å) SEDs of 81 galaxies for the investigation of the stellar population of LBGs. They employed the population synthesis model by Bruzual and Charlot (1996) with constant star formation rate and Salpeter IMF, a dust attenuation law by [Calzetti 1997]. Star formation histories considered were constant and exponentially declining ones ($\Psi = \Psi_0 \exp(-t/\tau)$) with τ ranging 10 to 100 Myr. They made fitting with three free parameters, namely, the time since the onset of star formation, the degree of dust extinction, and the star formation history as a function of time. The median of resultant ages (time from onset of star formation) was 320 Myr, and more than 25% of their sample galaxies turned out to be younger than 40 Myr. The dust extinction was generally moderate ($E(B-V) \sim 0.1$ – 0.4), and their typical stellar mass is estimated to be $\sim 10^{10}$ $M_\odot$, similar to a typical bulge mass of a present-day giant galaxy. [Papovich et al. 2001] used a sample of LBGs in the HDF-N with imaging data by HST/WFPC2 and NICMOS, as well as K_s-band images taken by the KPNO 4m telescope. Their sample consists of 33 galaxies at $2.0 \lesssim z \lesssim 3.5$. The updated version of population synthesis code by [Bruzual and Charlot 1993] (BC2001) was used, with an star formation history of the form $\Psi(t) = \Psi_0 \exp(-t/\tau)$ with $\tau = 0.01$-10 Gyr or an constant star formation rate. They tested two cases in metallicity and IMF; for metallicity they chose to use $Z = 0.2 Z_\odot$ and $1.0 Z_\odot$, and for the IMF those by Salpeter and by Scalo have been used. They found that mass estimates for an L^* galaxy in UV luminosity gave stellar mass $\sim 10^{10} M_\odot$ (they consider the mass estimates determined by their fit are minimum masses, because constant or declining SFR should give smaller mass-to-light ratio). The best-fitted ages of stellar population range from 30 Myr to ∼1 Gyr in most cases. They also examined two-component fitting with young stellar component plus maximally old stellar component, which was assumed to be formed at $z = \infty$. This two-component fitting gives upperlimit on the stellar mass in LBGs to be 6–8 times of the minimum mass estimates. The mass fraction of old stellar component is not so large in most cases, although the constraints are not tight. The choice of metallicity and IMF affect the result of fitting in some degree, but they argue that their main findings does not change. Interestingly, they pointed out that there is a clear deficiency of galaxies with red $V - H$ colors (figure 1 of [Papovich et al. 2001]). This suggests that massive galaxies with old stellar population is vary rare at $z \gtrsim 3$ (but see [Labbé et al. 2002]). Considering this with relatively smaller ages resulted from their SED fitting, they argue that a star formation in LBGs may not be well described by a simple continuous history as they have considered, but their evolutionary history is stochastic.

Metal abundance in ionized gas is estimated through rest optical emission line ratios to be sub-solar

similar to those of Large and Small Magellanic Clouds ([Teplitz et al. 2000]; [Pettini et al. 2001]). which is fairly high as compared with those obtained in damped Ly α systems derived from absorption line analysis.

On-going star formation rates estimated from emission lines in rest-frame optical band are up to several tens of $M_\odot$ yr^{-1}. [Pettini et al. 2001] reports that the estimation based on $H\beta$ luminosity does not show higher star formation rate than those by rest-frame UV luminosity more than a factor of 3, suggesting the absence of differential extinction between the rest-frame optical and UV wavelength.

To briefly summarize, the current observational results (such as number density, metallicity, stellar mass) seem to support the idea that the LBGs are the progenitors of massive galaxies at the present epoch. However, the details of evolutional process of these galaxies are still unclear. We still don't have clear answers for several questions; e.g., what kind of physics primary drives their star formation? How their star formation proceeds? Do they stop star formation at lower redshift? If so, when? What is the descendant of LBGs at $z \sim 1$? To answer these fundamental questions, larger number of data at wider range of redshift should be necessary, as well as an appropriate modeling of their evolution process.

1.1.3 Observations in Other Wavelengths

The recent development of instrumentations all over the wavelengths have enabled the examination of LBGs' properties in other wavebands through deep surveys. For example, [Brandt et al. 2001a] stacked the X-ray flux from 24 LBGs at $z \sim 3$ within the 1Ms Chandra Deep Field-North (CDF-N; [Brandt et al. 2001b]) and found a 3σ detection of soft X-ray. [Nandra et al. 2002] also made a stacking analysis using the CDF-N data for 144 LBGs without direct Chandra detection, and reported a 6σ detection. They argue that the X-ray luminosity of LBGs at $z \sim 3$ is about five times larger than that of Balmer-break galaxies at $z \sim 1$. It has been suggested that in the fainter flux range non-AGN star-forming galaxies contribute siginificantly to the X-ray background via high-mass X-ray binaries and type II supernovae. Thus examining X-ray properties of LBGs should provide important information both on the nature of X-ray background and star formation activity at high redshift.

On the other hand, deep observations in submillimeter wavelengths has revealed a population of dusty galaxies with large star formation rates, and their redshift are suggested to be $z > 2$ (e.g., [Smail et al. 1997]; [Smail et al. 2002]; [Barger et al. 1999]). The relationship between these dusty galaxies at high redshift and LBGs remains unclear. Recently [Webb et al. 2003] placed an upper limit on the contribution from LBGs to submillimeter background of ∼20 %. They also argue that there is a significant spatial correlation between the LBGs and submillimeter sources. [Ouchi et al. 1999] argue that the dust temperature in LBGs seems to be higher ($\gtrsim$ 40K) than local optical and infrared-selected galaxies, and it may be due to the effective dust heating by massive star formation or to the difference in the dust properties.

1.1.4 Star Formation Density and Comparison with Theoretical Models

The LBGs make the statistical sample of UV luminous objects at high redshift. Since the UV luminosity density is considered to be correlated with the star formation rate per unit volume, the LBGs have opened up the possibility to examine the star formation history in the early universe (Madau et al. 1996, 1998). [Steidel et al. 1999] found that the UV luminosity density at $z \sim 4$ is almost comparable to that at $z \sim 3$. If the correction for the dust extinction is applied, the star formation densities at $z = 3$ and 4 are comparable to the value at $z = 1 - 2$. The similarity of the luminosity function of LBGs at $z = 3$ and at $z = 4$ and the rather flat (extinction corrected) star formation density history in $1 < z < 4$ are quite interesting and may be a key property to understand star formation history of galaxies. As mentioned above, the ages of the LBGs at $z = 3$ are estimated to be 10 Myr to 1 Gyr with a median value of 0.1–0.3 Gyr based on the SED fitting analyses by assuming a continuous star formation. If these ages can be regarded as time intervals from the onset of the first star formation, the LBGs at $z \sim 3$ should be much young and most of them should form at $z < 4$ (e.g., [Papovich et al. 2001]). Accordingly, the star formation density contributed by the LBGs at $z \sim 3$ should be lower by a factor of about 10

at $z > 4$ [Ferguson et al. 2002] and the LBGs at $z \sim 3$ must be different from the LBGs at $z \gtrsim 4$. Alternatively if the star formation of an individual galaxy is sporadic, this would not be the case.

By using semi-analytic models based on the hierarchical clustering scenario, several authors have tested whether the observed number densities and star formation densities at $z \sim 3$ and $z \sim 4$ can be reproduced. Based on the hierarchical clustering scenario [Mo and Fukugita 1996] estimated the number density of dark halos on the basis of Press-Schechter formalism with several variations of cold dark matter (CDM) cosmological models, and showed that the abundance of LBGs at $z \sim 3$ can be used to discriminate the plausible formation scenario. [Baugh et al. 1998] found that the abundance of LBGs at $z \sim 3$ can be reproduced with a reasonable choice of parameters, which are chosen to match with the observed properties of galaxies in the local universe. They further predicted that the UV luminosity density has a peak at $z = 1$–2 and decays with increasing redshift in $z > 2$; the predicted star formation density at $z = 5$ is comparable to that at $z = 0$. [Somerville et al. 2001] examined nature of these LBGs using their own semi-analytic models including starburst induced by collision of galaxies. Their model reproduces the observed luminosity functions of LBGs both at $z = 3$ and $z = 4$ with a reasonable amount of dust extinction, and the estimated star formation density are claimed to be compatible with observations.

1.2 Objective of the Present Study

As a next step to these studies of Lyman break galaxies at $z \sim 3$ to 4, we should make a exploration of the earlier universe aiming to the disclose nature of higher redshift galaxies. The extension of the observational data toward higher redshift provides a stronger constraint on physical processes of the galaxy evolution through the comparison with theoretical models. It is also indispensable to study the epoch of the generation of the first galaxies. The study at the higher redshifts has a further importance because it is approaching to a suggested epoch of the cosmological reionization ($z \gtrsim 6$; [Becker et al. 2001]). The number densities of the LBGs may provide a constraint on determining the contribution of the star forming galaxies to the ionizing background radiation [Madau et al. 1999]. The discoveries of several star forming galaxies at $z \gtrsim 5$ have been already reported (e.g., [Dey et al. 1998]; [Weymann et al. 1998]; [Spinrad et al. 1998]; [Dawson et al. 2001]; [Ellis et al. 2001]; [Dawson et al. 2002]). Their properties are important in the context of the investigation of the nature of galaxies at high redshift. However, since there has not been a volume-limited large sample, statistical properties of galaxies at $z \sim 5$ remain unknown. Finding many galaxies at $z \sim 5$ systematically and studying their statistical nature is necessary for the first step. We should carry out a survey with a sufficiently large search area at a deep limiting magnitude. However, it is not easy in technical aspects. The distance to the objects are getting larger and thus apparent magnitude and surface brightness are getting fainter. Consequently a number density at an apparent magnitude decreases rapidly. In addition, the observing band shifts to the redder wavelength region where OH sky emission increases the background noise. Therefore a large aperture of a telescope and a wide field of view are required to perform this task.

Here we present the first results of our survey of LBGs at $z \sim 5$ using the Subaru Prime Focus Camera (Suprime-Cam; [Miyazaki et al. 1998]; [Miyazaki et al. 2002]), utilizing its unique capability of a wide field of view among 8m class telescopes. We choose the sky area including the Hubble Deep Field-North (HDF-N), because there are plenty of information of galaxies with a wide redshift range ($0 < z < 6$). This database is quite powerful to examine our method for searching for galaxies at $z \sim 5$ and to obtain a reliable sample of candidates, under the circumstances that considerably time consuming optical follow-up spectroscopy must be carried out after making a candidate catalog. The field is also the sky area where many deep surveys in variety of wavelengths such as X-ray, infrared and radio. We will be able to utilize these data to investigate nature of LBG population in other wavebands.

In chapter 2, the filter selection, imaging observations and details of the basic data analysis is described. In chapter 3, criteria for finding LBGs at $z \sim 5$ and the number of objects detected are presented. Properties of the LBG candidates are also described. Then in chapter 4, we quantify the corrections needed to apply to the observed data for deriving the luminosity function, and the resultant luminosity function of LBGs at $z \sim 5$ is presented. In chapter 5, implications of our findings to the evolution process of LBGs, as well as the comparison of the observed cosmic star formation history and

the model predictions are discussed. The contribution of LBGs at $z \sim 5$ to the UV ionizing field is also mentioned. In chapter 6 we give a conclusion of our findings and some prospects for future works as a direct extension of the current study.

We use a set of cosmological parameters of $H_0 = 65$ km s^{-1} Mpc^{-1}, $\Omega_{\rm M} = 0.3$, and $\Omega_\Lambda = 0.7$ as a primary set, and in some cases we also use an Einstein-de Sitter universe model with $H_0 = 50$ km s^{-1} Mpc^{-1}, $\Omega_{\rm M} = 1.0$ and $\Omega_\Lambda = 0$ which had been commonly used as a standard set of cosmological parameters. The magnitude system is based on Vega magnitude except for the cases otherwise noted.

Chapter 2

Observations and Data Reduction

2.1 Filter Selection

Prior to the observation, the combination of the filters suited to isolate the $z \sim 5$ population was explored using mock galaxy spectra constructed with stellar population synthesis codes. Although it is not obvious that SEDs of LBGs at $z \sim 5$ are similar to those at $z \sim 3$, we adopted model SEDs of LBGs at $z \sim 5$ to enclose various rest-frame UV SEDs of LBGs at $z \sim 3$. The model spectrum for young, actively star-forming galaxies, by which we intend to model the SED of LBGs with the bluest UV color, was constructed using the stellar synthesis code developed by [Kodama and Arimoto 1997]. We included the attenuation due to the inter-galactic medium following the prescription by [Madau 1995]. In order to have the model spectra to delineate the redder SED of LBGs, we adopted to take into account the reddening effect by dust within the object itself using the extinction curve given by [Calzetti et al. 2000] with $E(B-V)$ from 0.0 to 0.4. In figure 2.1 we show the SEDs of the model spectra with $E(B-V) = 0.0$, 0.2 and 0.4, as well as the rest-frame photometric data points of LBGs at $z \sim 3$ in the HDF-N [Papovich et al. 2001]. The model spectra reasonably cover the UV colors of the LBGs at $z \sim 3$. The adoption of the dust extinction is rather arbitrary to reproduce the redder colors of LBGs. The interpretation is, however, often used to derive color excesses in LBGs (e.g., [Steidel et al. 1999]).

We also prepared model spectra of spiral and elliptical galaxies for examining the efficiency of eliminating galaxies at intermediate redshifts. As spectra of spiral galaxies we used those of Sbc and Scd galaxies derived by [Coleman et al. 1980]. As a spectrum of an elliptical galaxy we employed the model spectrum by [Kodama and Arimoto 1997] which reproduces the color-magnitude relation of elliptical galaxies observed in the local universe. Then we calculated observed spectra for each type of galaxy from $z = 0$ to $z = 6$ with a step of 0.1. We did not consider any effect of evolution for all types of galaxies.

A desirable combination of the filters should give the most distinct separation of the $z \sim 5$ population apart from the objects with smaller redshifts. We chose a combination of V, I_c, and z'-bands. In the figure 2.2a, we show the two-color $V - I_c$ versus $I_c - z'$ diagram. It is seen that galaxies at $z > 4.5$ can be well separated from foreground objects in the diagram. The most critical contamination is caused by elliptical galaxies at $z \sim 0.5$ due to the 4000 Å break and early type spirals at intermediate redshifts.

Selecting R-band instead of V-band may also be reasonable, because of the high quantum efficiency at the band. However, contamination by galaxies with 4000 Å break at intermediate redshifts is more serious than the adopted filter combination. Another reason we did not choose R-band is less continuum depletion by Lyman alpha forests.

2.2 Observations

The observations were carried out on 22nd and 23rd February, 2001 with Suprime-Cam attached to Subaru telescope at Mauna Kea. The Suprime-Cam consists of 10 mosaiced CCDs, each of which has a dimension of 2046 by 4090 pixels with a pixel scale of $0.''2$. Each CCD covers a field of $\sim 7'$ by $\sim 13'$ and a typical gap between the CCDs is $10'' - 15''$. The details of the observation are summarized in table 1. Note that our observations were made before the upgrade of the CCD array configuration held on April 2001, and the one CCD chip (at the north-west corner) was not working and another chip (at the

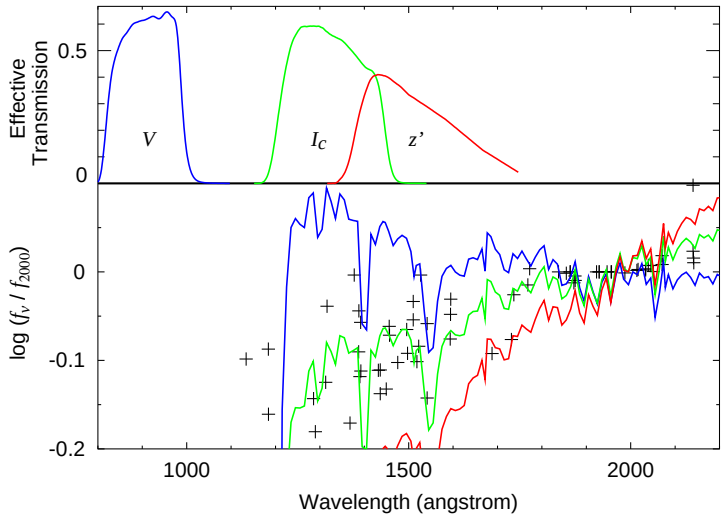

Figure 2.1: Model UV spectra of LBGs at $z \sim 5$, which are used for the filter selection and for the evaluation of the incompleteness of our survey via Monte Carlo simulation (in section 5.2). The bluest (extinction-free) spectrum is shown in the blue solid line. The green and red lines are spectra of the redder LBGs attenuated by dust with $E(B-V) = 0.2$ and 0.4, respectively. The attenuation by the intergalactic matter is taken into account (Madau et al. 1996). Points are photometric data of the LBGs in the HDF-N at $z \sim 3$ [Papovich et al. 2001]; we intend to cover the various SEDs at $z \sim 3$ by model spectra. All flux densities are normalized at 2000 Å. In the upper side of the figure we show the effective band-passes of the Suprime-Cam with V, I_c and z' filters, which are blueshifted as they work for an object at $z = 5$.

south-west corner) had many bad columns. Thus 8 CCDs were effectively working, and about $\sim 27'$ by $\sim 27'$ field is covered by a frame.

The imaging observation was made pointed to the Hubble Deep Field-North (RA(2000) = 12h36m49s.4, Dec(2000) = +62D12'58"). Images were taken with a small dithering (typically $20''$) with a typical exposure time of 1440 sec, 180 – 240 sec, and 120 sec, for V, I_c, and z'-bands, respectively for each exposure. A seeing size during the observations was typically $\sim 0''.9$ and we discarded some exposures with a median FWHM of stars larger than $1''.0$ for keeping the angular resolutions of the final images. Effective integration times were 21.6 ksec, 2.5ksec, and 3.1 ksec for V, I_c, and z'-bands, respectively.

2.3 Data Analysis

2.3.1 Basic Data Reduction

The data reduction was carried out in a standard manner using IRAF[1] for basic data processing; bias was subtracted using counts in an overscan region, flat field frames were made by using normalized average of the object frames. The data processing was made by the combination of IRAF cl scripts and perl scripts (partly in C) written by us, which enabled semi-automatic processing (processing was made automatically after setting some data properties such as bad pixels, overscan regions, masks for bright sources, and stars to be used for seeing and flux adjustments). A flow-chart of data processing for one CCD chip, one filter image is shown in figure 2.3. The sensitivity differences between the CCD chips have been corrected using the relative count rates of the flat-fielded dome flat frames for all three bands. The background was subtracted by two dimensional polynomial fitting. Positions of the frames are aligned by measuring the positions of the field stars appeared commonly in all exposures and fitting fourth-order polynomial functions for coordinate conversion. All images were aligned to the I_c-band fiducial frame, in order to

[1]IRAF is distributed by the National Optical Astronomy Observatories, which are operated by the Association of Universities for Research in Astronomy, Inc., under cooperative agreement with the National Science Foundation.

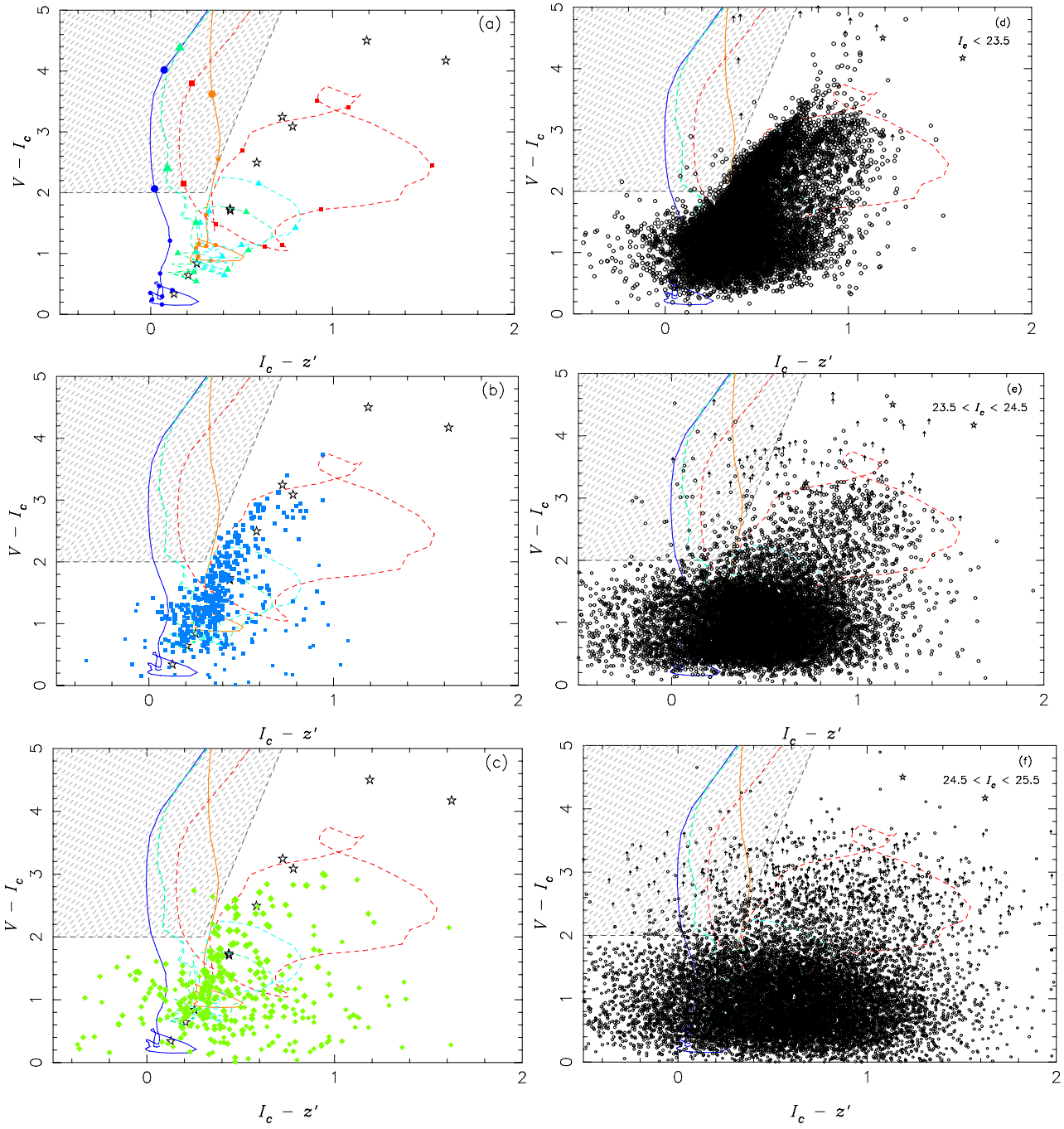

Figure 2.2: $I_c - z'$ versus $V - I_c$ diagrams. **(a):** Tracks of colors for model galaxies at redshift ranging from 0 to 5.5. A blue (an orange) line represents a galaxy with the bluest (reddest) model spectrum, i.e., $E(B-V) = 0.0$ ($E(B-V) = 0.4$) (see figure 2.1). A green and cyan dashed lines refer to local spiral galaxies (green is for Sbc, and cyan is for Scd; [Coleman et al. 1980]). A red dashed line is for a local elliptical galaxy. No evolution is considered. The symbols are plotted at a redshift interval of 0.5, and the symbols at $z \geq 4.5$ are enlarged. Star-symbols indicate the colors of A0 – M9 stars calculated based on the library by [Pickles 1998]. Hatched region indicates the color criteria we adopted for $z \sim 5$ galaxies. **(b):** Colors of galaxies cataloged in the spectroscopic survey of galaxies in the HDF-N and its flanking fields by [Cohen et al. 2000] and identified in our image. All galaxies with the redshift range $z < 4.5$ are plotted. Tracks for model spectra are also shown. **(c):** Same as (b), but for galaxies in the HDF-N for which the photometric redshifts are given by [Fernández-Soto et al. 1999] as $z < 4.5$. **(d) – (f):** The color distribution of the sources extracted from our image. Panels (d), (e) and (f) show objects with $I_c \leq 23.5$, $23.5 < I_c \leq 24.5$ and $24.5 < I_c \leq 25.5$, respectively. Circles are objects detected in all of V, I_c, and z'-bands, and arrows are those detected in I_c and z' but not in V-band. Lower limits of $V - I_c$ colors are given for them.

Table 2.1: Details of the observation.

Dates	22 and 23 Feb. 2001		
CCD dimension	9 CCDs with 2046 × 4090 pixels		
Pixel scale	$0.2''$/pixel		
Field of view / Effective surveyed area[∗]	836 arcmin^2 / 575 arcmin^2		
Filters	V	I_c	z'
Effective integration time	21,600 sec.	2,520 sec.	3,100 sec.
Seeing	$0''.8$ – $1''.0$	$0''.7$ – $1''.0$	$0''.6$ – $1''.0$
Limiting magnitude[†]	28.5 mag.	25.5 mag.	25.2 mag.

∗: The effective surveyed area represents the area used to derive the luminosity function.
†: The magnitude of the faintest object that can achieve S/N of 5 with the typical aperture size corresponding to the area of the detected sources at the magnitude range ($0.''9$ for V and z'-bands, $1.''2$ for I_c-band).

improve the accuracy of the object detection which selected objects appeared in two (I_c and z') or three bands. Counts of each frame were adjusted by comparing the count-rate of the field stars common to all exposures for every filter; we measured the counts of field stars in each frame, then the images were divided by the median of the count ratios of stars relative to a fiducial frame so that the count of stars are almost constant among exposures.[2] After the adjustment of seeing size by the convolution, the frames were stacked with a sigma-clipping algorithm.

2.3.2 Photometric Calibration

Photometric calibrations for V and I_c-band images were made using images of photometric standard stars in [Landolt 1992]. The accuracy was ~ 0.02 mag for V and ~ 0.08 mag for I_c. For the photometric calibration of the z-band images, we employed two ways both based on the $I_c - z'$ color. We first set an arbitrary zero point for z' magnitude. In the first method, we examined the distribution of $V - I_c$ and $I_c - z'$ colors of field stars exposed on our images. Next we calculated the $I_c - z'$ colors to be observed with the system sensitivity of Suprime-Cam for the stars in the stellar flux library by [Pickles 1998]. We can determine the magnitude zero point for z'-band by comparing the distribution of these colors. Another method is to use the spectral energy distribution of the galaxies in the HDF-N and its flanking fields. We used the galaxies for which the published V, I and J-band magnitudes are available and estimated their $I_c - z'$ colors by linear interpolation. We adopt the magnitude zero point determined by the latter method. The z' magnitude zero points derived by these two methods agrees within ~ 0.1 mag in the color range of $I_c - z'$ between ~ 0 and 1. In figure 2.4 we show the difference of $I - z'$ colors in our image and published colors for galaxies in the HDF-N along with their published I-band magnitude, as well as the $V - I_c$ and $I_c - z'$ color distribution of stellar flux data in [Pickles 1998] and stars in our images. The z'-band magnitude is also based on Vega. We used the flux density table of Vega given by [Castelli and Kurucz 1994], and applied z'(AB) - z'(Vega) = 0.5505. In figure 2.5 we show the $V - I_c$ and $I_c - z'$ colors of stellar like sources in all CCD chips. This figure indicates that the sensitivity adjustment between different CCD chips and different filter bands works correctly, except one CCD chip where many bad column are present and possibly has irregular sensitivity. We do not use the objects included in this CCD chip for the statistical analyses such as calculation of luminosity function.

The conversion equations from count rate of the final image to Vega based magnitude in three bands are as follows (cts_*^{-1} is a count rate in a second in each band):

[2] In this procedure, we found that although the variance of the flux ratios is stable and is well correlated with the airmass of the observed sky region on 23rd Feb, the flux ratio varies largely and the correlation of the flux ratio and the airmass is weaker on 22nd Feb. This suggests that the sky condition of the second observing night was better than the first night. Thus we selected one frame per filter as a fiducial frame, which was taken on the second night and the observed time is close to that of the exposures for standard stars. We adjusted the count-rate of the frames taken on the first night and other frames taken on the second night according to the fiducial frame.

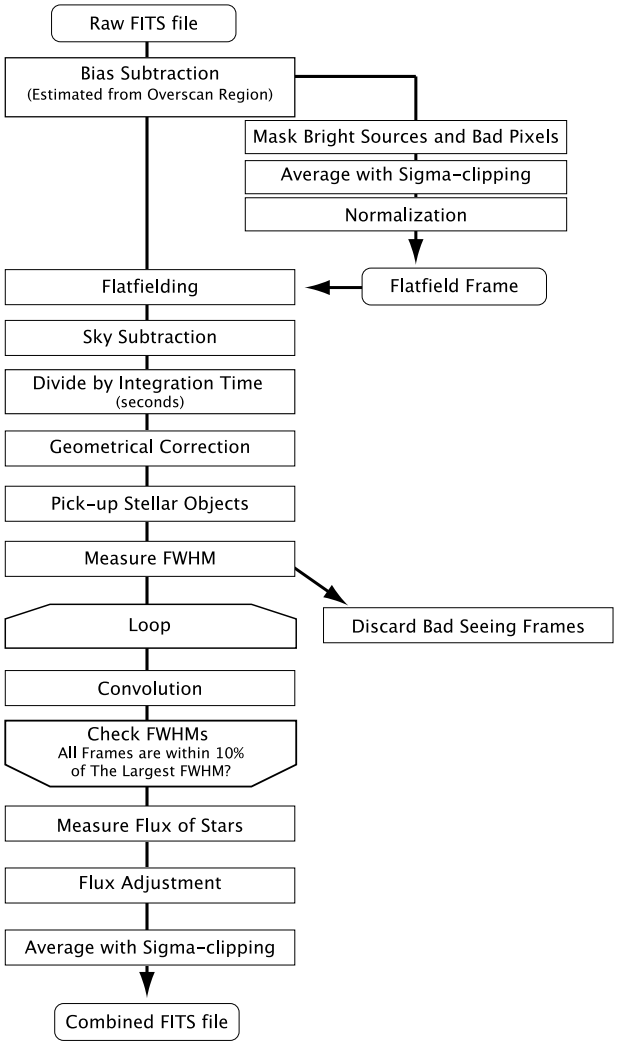

Figure 2.3: A schematic diagram of one CCD chip and one band image processing.

$$V = 27.789 - 2.5\log(cts_V^{-1}), \tag{2.1}$$

$$I_c = 27.136 - 2.5\log(cts_{I_c}^{-1}), \tag{2.2}$$

and

$$z' = 26.121 - 2.5\log(cts_{z'}^{-1}). \tag{2.3}$$

In these equations we did not include color-correction terms, because the results of fitting by standard stars returned color-correction factors for V, and I_c data are smaller than fitting errors.

2.3.3 Source Detection and Cross-identification with the HDF-N

Prior to the extraction of the astronomical objects from the final imaging data, we set masks for source detection around the bright objects in order to avoid the misidentification of the noise or tails of the bright objects as an individual object. We also removed the edge regions of each CCD chip from the object detection because of their low signal-to-noise ratio caused by dithering imaging. In total 26.1 % of the CCD chip area is masked, and the effective area observed is 618.6 arcmin^2 (575.0 arcmin^2 without the CCD chip with many bad columns).

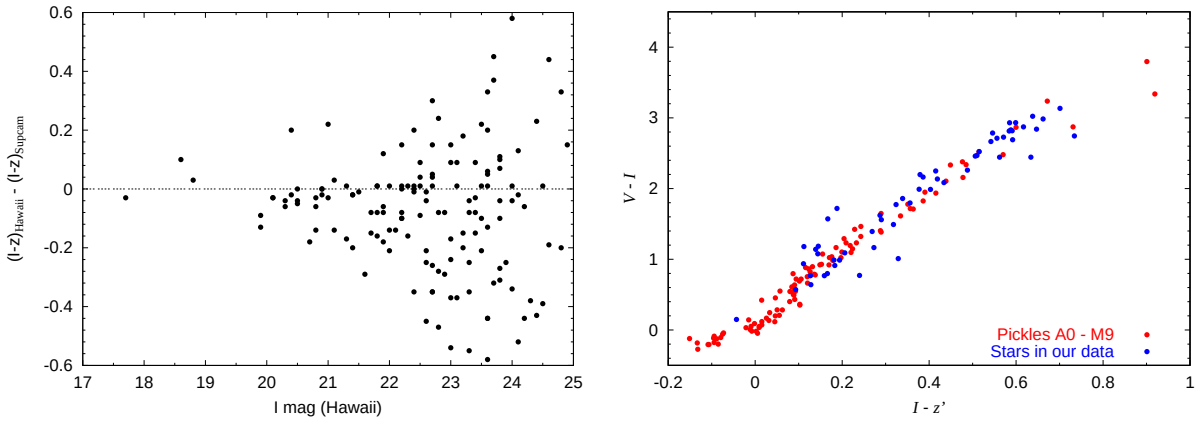

Figure 2.4: **Left panel**: Differences of $I - z'$ colors in our image and published colors (estimated by interpolation with I and J-band data) for galaxies in HDF-N. **Right panel**: Comparison of $I_c - z'$ and $V - I_c$ colors of stars in the stellar flux library by [Pickles 1998] and objects with stellar appearance and with $I_c < 21$. z'-band magnitudes of stars in our images are calibrated by the colors of HDF-N galaxies. Stars in our image shown here are in a CCD chip which include the field of the HDF-N.

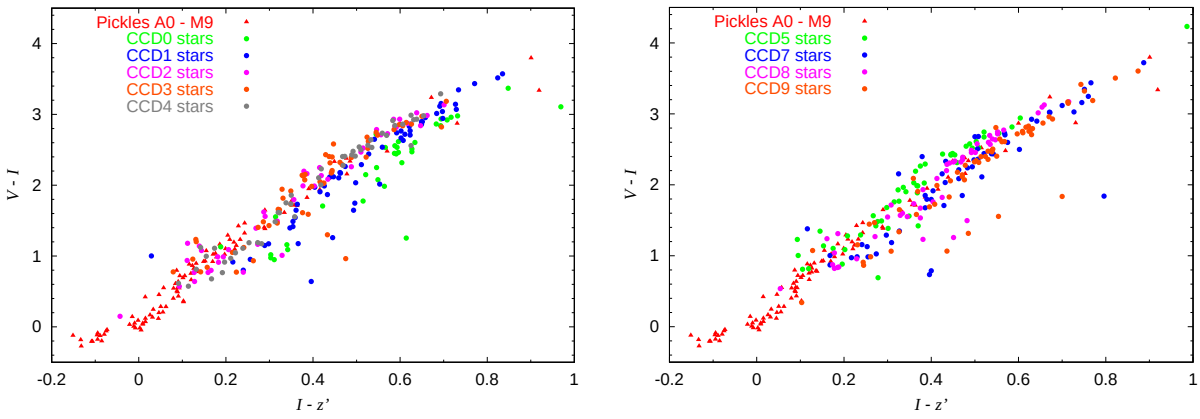

Figure 2.5: **Left panel**: Same as figure 2.4 (right panel), but colors of stars in 4 CCD chips are plotted as well as colors of stars in the stellar flux library by [Pickles 1998]. "CCD0" is a CCD with many bad columns. Stars in the CCD show relatively large deviation, indicating the calibration for the CCD chip does not work well compared to other CCD chips. **Right panel**: Same as the left panel, but for the remaining 4 CCD chips.

Table 2.2: The I_c-band number count.

Magnitude range (I_c)	Detected Number	$\log(N_{raw})$ [$*$] [mag^{-1} deg^{-2}]	$\log(N_{corrected})$[†] [mag^{-1} deg^{-2}]
23.0 – 23.5	3184	4.60	4.62
23.5 – 24.0	4430	4.74	4.76
24.0 – 24.5	5917	4.87	4.95
24.5 – 25.0	6596	4.92	5.09
25.0 – 25.5	6122	4.88	5.43

$*$: Number count in our I_c-band images (8 CCD chips), not corrected for incompleteness.
†: Number count corrected for incompleteness, according to the result of comparison with HST/WFPC2 $I(814)$ image.

We used the software SExtractor [Bertin and Arnouts 1996] for the source detection and photometry. The primary parameters for the object detection are the threshold of count above which the pixel is treated as a part of an object and the minimum number of connected pixels to be classified as an object. We extensively examined these parameters by comparing the detected sources with the objects in the HDF catalog version 2 [Williams et al. 1996] brighter than $I_{\rm AB}(814) = 27$, to minimize both the rate of noise contamination and the rate of missing objects. We also tested some spatial smoothing filters and adopted a Gaussian smoothing filter with a FWHM of 3 pixels for I_c and z'-bands.

The best set of parameters with which the detection rate of faint objects and the noise contamination are compromised is that the thresholds are 1.3, 1.0, 1.0 times of background noise for V, I_c and z', respectively and to have at least 4 connected pixels above threshold in each band. (1.0 sigma noise per pixel corresponds to 29.0 mag arcsec^{-2}, 26.9 mag arcsec^{-2}, and 26.0 mag arcsec^{-2} in V, I_c, and z'-bands, respectively.) We pick out objects only if they are detected both in I_c and z'-bands. The number of sources thus selected is 29,094 for $I_c \leq 25.0$ and 35,362 for $I_c \leq 25.5$ in the 9 CCD chips. Although the adopted detection criteria seem to be loose, i.e., seem to tend to pick out many noises, the criterion of two band detection removes noises efficiently. In fact, there is no misidentification of noise as an object in $I_c \leq 24.5$ and the number of the noise misidentification in $24.5 < I_c \leq 25.0$ is two among 55 extracted sources within the HDF-N region. Even in the magnitude range $25 < I_c \leq 25.5$, which is the faintest range we use, the rate of misidentification of noise is not so large; it is $\sim 17\%$. The number of selected sources are robust for changes of the detection parameters; if we adopt 10 pixels for the minimum connection of pixels for V and I_c-bands, we only lose $\sim 2\%$ of the objects at the faintest magnitude range. Vast majority of selected objects have area larger than 10 pixels in I_c-bands. The fraction of selected objects in our image among the HDF-N catalog is getting smaller as the magnitude goes fainter; ~ 100 % for $I_{\rm AB}(814) \leq 25$, ~ 67 % for $25 < I_{\rm AB}(814) \leq 25.5$, ~ 28 % for $25.5 < I_{\rm AB}(814) \leq 26.0$. The detection rates in other CCD chips do not change much as described in section 4.1. The number counts in I_c-band are presented in 2.2. In figure 2.6 we show our I_c number count, compared with [Tyson(1988] and [Williams et al. 1996]. If we correct the incompleteness of our source detection, the number counts of our data agree well with those appeared on previous studies.

Photometry of the detected objects was also made using SExtractor. We use the value "best magnitude" in SExtractor for I_c magnitude and a $1''.6$ aperture magnitude for $V - I_c$ and $I_c - z'$ colors. The photometric accuracies were estimated by putting many artificial objects randomly into our final images. The size parameter was adjusted so that the obtained distribution of sizes and apparent magnitudes of artificial objects resembles to that of real galaxies in all of three bands. The procedures of object detection and photometry are same as those for the observed data. The rms errors of I_c-band "best magnitude" for objects with $24.0 < I_c \leq 24.5$, $24.5 < I_c \leq 25.0$ and $25.0 < I_c \leq 25.5$ were 0.28, 0.35 and 0.41 mag, respectively. These error values are roughly consistent with the errors of I_c magnitude estimated from the comparison with the I_{814} magnitude for the objects in the HDF-N region. Photometric errors for V-band data is 0.22, 0.31 and 0.33 mag for $26 < V \leq 26.5$, $26.5 < V \leq 27.0$ and $27.0 < V \leq 27.5$, respectively,

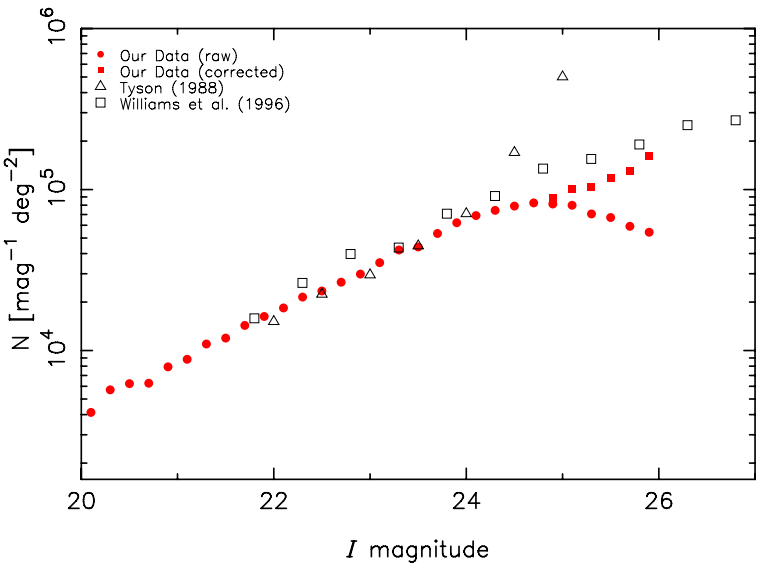

Figure 2.6: Galaxy number counts in I-band. Solid circles show number count in our I_c-band image, without completeness correction. Corrected number counts in $25 < I_c < 26$ are shown by solid squares. The completeness correction factor was determined by the comparison with HST/WFPC2 $I(814)$-band image. Open triangles and open squares are counts by [Tyson(1988] and by [Williams et al. 1996], respectively. $I(814)$ number counts by [Williams et al. 1996] are converted to Vega system.

and for z'-band data, 0.39 mag, 0.45 mag and 0.49 mag for $23.5 < z' \leq 24.0$, $24.0 < z' \leq 24.5$ and $24.5 < z' \leq 25.5$, respectively. The errors in $V - I_c$ and $I_c - z'$ colors, which were measured with a $1''.6$ aperture magnitude, are smaller than the errors in the total magnitude; it is typically 0.08 mag and 0.11 mag for $V - I_c$ and $I_c - z'$ colors, respectively, for objects with $23.0 < I_c \leq 23.5$, and 0.4 mag and 0.5 mag for $V - I_c$ and $I_c - z'$ colors, respectively, for objects with $25.0 < I_c \leq 25.5$.

In figure 2.7 the distributions of the size of objects detected in three bands are presented as a function of their magnitude. The size of an object was calculated from the number of pixels above the detection threshold in each band, under the approximation that the object has a round shape. The size of the objects with $24 < I_c \leq 24.5$ is 8 to 10 pixels, and the objects with faintest magnitude range have ~ 4 pixels diameter in V and I_c-bands, where in z'-band the sizes are often smaller than the seeing size. The background noise levels were measured by counting flux with different aperture diameters. By this procedure we found that the background noise (the fluctuation of background counts) increase more rapidly than it is expected for the Poisson noise. We show in figure 2.8 the rms background noise as a function of aperture diameter for I_c-band image. Similar tendency also exists in V and z'-bands. The fact that the background noise increases rapidly with increasing diameter suggests the existence of the fluctuation of background noise in large scale. Although there are some possible causes, e.g., instrumental noise or the intrinsic fluctuation of the cosmic background light originated from objects with very small flux, we could not figure out the origin of this noise behavior. If we consider the typical sizes of objects according to the magnitude of an object (see figure 2.7), the photometric errors measured by putting artificial objects described above are consistent with the background noise measurements.

2.3.4 Astrometry

The astrometry for detected objects were made using stars in our field-of-view listed in APM sky catalog [Irwin et al. 1994]. We added stars from USNO-A2.0 [Monet et al. 1998] to increase the number of stars for calculation of conversion coefficients. There is no systematic error larger than $0.''3$ between these two catalogues in our region. We measured the positions of the stars in our I_c-band final image and fitted a fourth-order polynomial function to minimize the χ^2 of the positional errors, for conversion of positions in our images to equatorial coordinates. The relative positions of CCD chips were also adjusted to provide a minimum error for the coordinate conversion. The achieved internal positional accuracy was

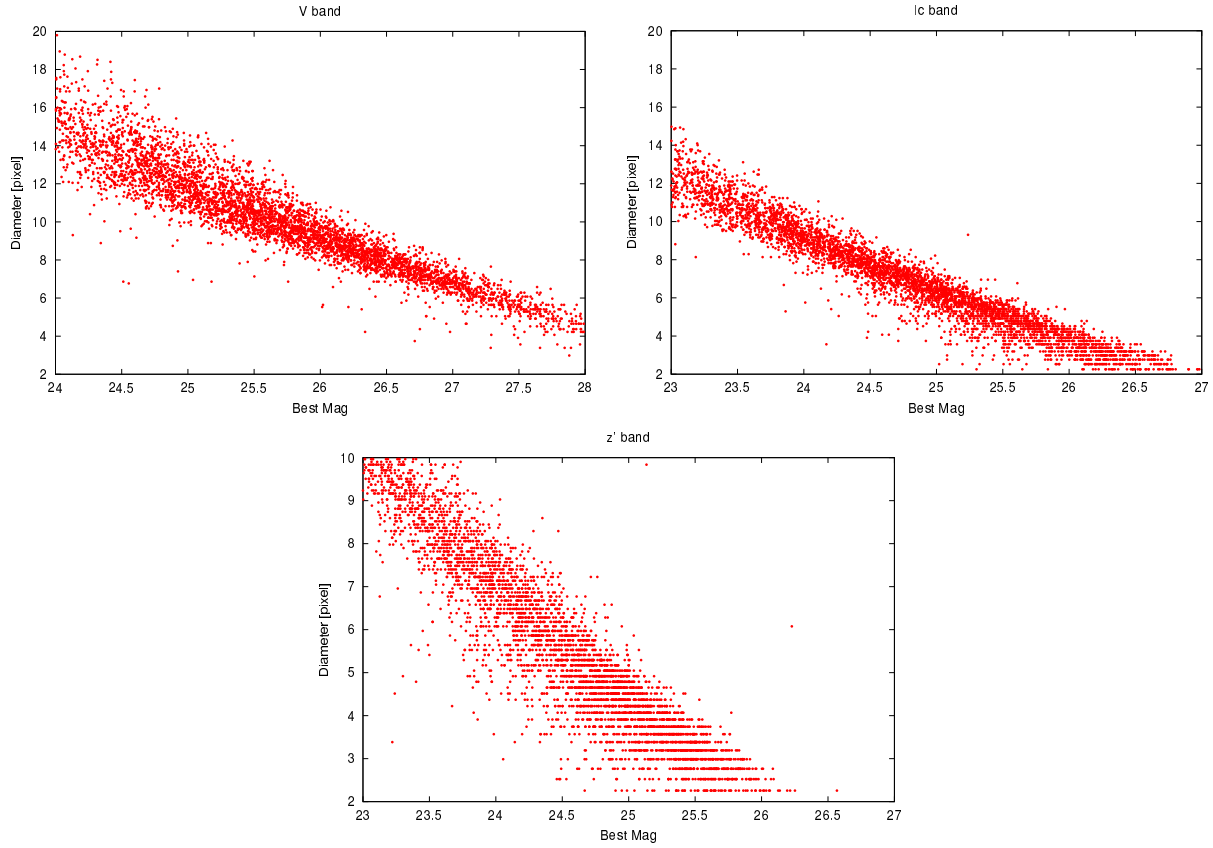

Figure 2.7: The size distribution of the detected objects according to their magnitudes. From left to right, the distributions in V-band, I_c-band, and z'-band are shown. The size of the objects are shown as a diameter in pixels, which was calculated from the number of pixels above the detection threshold in each band (One pixel corresponds to $0''.2$).

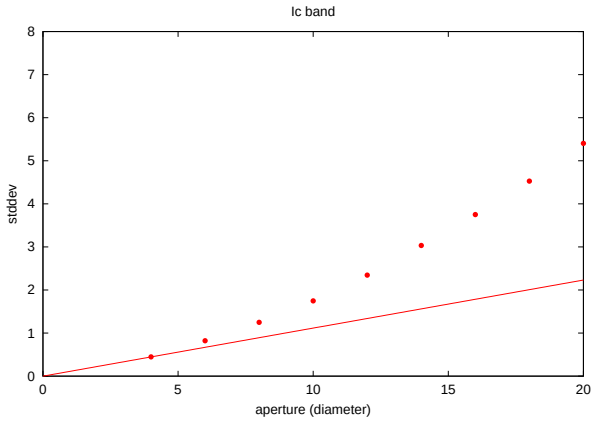

Figure 2.8: The 1σ background noise with varying aperture size, in I_c band image. The points indicate the rms background noise with different apertures (the unit is counts per second). The unit of horizontal axis is pixels. The line shows the expected background noise if the background noise is Gaussian, based on the rms value at an aperture of 4 pixels ($=0.''8$) diameter.

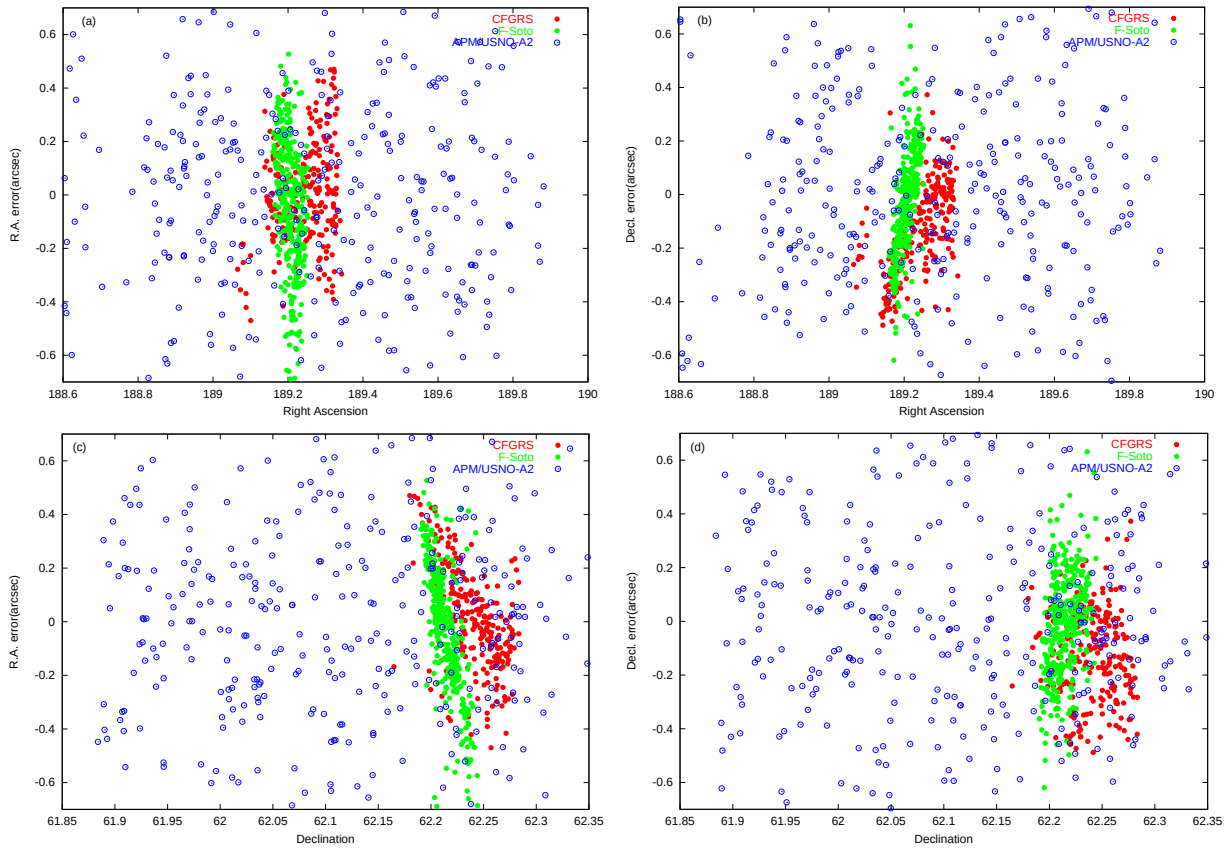

Figure 2.9: Positional errors of stars in APM sky catalog or USNO-A2.0, which are identified in our images (open circles). Red and green circles indicate the difference in positions in our data and those in published catalogues for galaxies in CFGRS [Cohen et al. 2000] and in photometric redshift catalog of galaxies in the HDF-N [Fernández-Soto et al. 1999].

$\sim 0''.4$ rms for most part of the image. In figure 2.9 we show the resultant positional errors for 317 stars in our image, which are cataloged in APM sky catalog or USNO-A2.0. There is no significant systematic error which depends on the sky position. We also show in the figure the positional errors of galaxies in CFGRS [Cohen et al. 2000] and HDF-N photometric redshift catalog [Fernández-Soto et al. 1999]. There are systematic errors between these catalogues and positions in our data, particularly seen in the panels for Right Ascension versus Declination residuals and for Declination versus Right Ascension, although the size of positional errors are smaller than those achieved by the calibration using APM and USNO-A2.0.

Chapter 3

Selection of LBG Candidates at $z \sim 5$ and Their Properties

3.1 Selection of LBGs at $z \sim 5$

One of the most serious problems in the study of statistical properties of Lyman break galaxies is a certain amount of contamination by objects located between us and objects at the targeted redshift (so called 'interlopers'). The uncertainty of the fraction of the contamination affects the reliability of statistical properties of the population, such as the luminosity function or the amplitude of the clustering. In figure 2.2a, we can see that a galaxy with an old stellar population (red dashed line) at $z \sim 0.5$ is close to the selection window for $z \sim 5$ galaxies; the 4000 Å break in a galaxy at $z \sim 0.5$ mimics the color by the Lyman break at $z \sim 5$.

3.1.1 Cross-identifications of Galaxies at Intermediate Redshifts

In order to determine the selection criteria for galaxies at $z \sim 5$ as reliable as possible, we have utilized the previously published redshift data of the HDF-N and its flanking fields. We used the list of galaxies in the HDF-N and the flanking fields by Caltech Faint Galaxy Redshift Survey (CFGRS; [Cohen et al. 2000]) and the catalog of photometric redshift of galaxies in the HDF-N by [Fernández-Soto et al. 1999]. The magnitude limit is $R \sim 25.5$ mag for the CFGRS catalog and $I_{\rm AB}(814) = 28.0$ mag for the photometric redshift catalog. We find 566 galaxies out of the 671 galaxies in the CFGRS catalog and 317 galaxies out of the 477 galaxies with $I_c < 26$ and at $z < 4.5$ in the photometric redshift catalogue. Most of the galaxies in the CFGRS catalog which have no counterpart in our image are located outside of our final image (between CCD chips or in the masked regions). Galaxies listed in the catalog by [Fernández-Soto et al. 1999] but not in our image are objects fainter than our limiting magnitude. In figure 2.2c and 2.2d, we plot the colors ($I_c - z'$ and $V - I_c$) of thus identified galaxies at $z < 4.5$ in the CFGRS sample and in the photometric redshift sample, respectively.

3.1.2 Color Selection Criteria

Considering the distribution of the foreground galaxies in the two color diagrams we adopt the selection criteria for galaxies at $z \sim 5$ as

$$V - I_c \geq 2.0, \tag{3.1}$$

and

$$V - I_c \geq 7(I_c - z') - 0.1. \tag{3.2}$$

The selection window defined by these criteria is shown as a hatched region in figure 2.2. There is no galaxy in the selection window in the spectroscopic redshift database with $z < 4.5$ and only two galaxies

in the photometric redshift database estimated to be at $z < 4.5$. These two galaxies are HDF 3−0238.0 and HDF 4−0505.1. The I_c magnitude of HDF 3−0238.0 in our image is 24.8 mag and its position in the two color diagram is close to the boundary of our selection criteria. It is classified as an elliptical galaxy at $z = 0.92$ by [Fernández-Soto et al. 1999] and has a round shape both in drizzled HDF-N image and in our I_c-band image. The estimated redshift of HDF 4−0505.1 by [Fernández-Soto et al. 1999] is 1.44. It is associated with a more extended object HDF 4−0505.0, for which the photometric redshift is not available and it has similar colors to HDF 4−0505.1. Our I_c-band image cannot resolve these two objects. These objects could be interlopers which happen to enter our color selection window.

In figure 2.2d–f the color distribution of the all detected objects is shown, separately with three magnitude bins: $I_c < 23.5$, $23.5 < I_c \leq 24.5$, $24.5 < I_c \leq 25.5$. For objects which are not detected in V-band, we assign the lower limit of $V - I_c$ color using the limiting V magnitude of 28.5 mag. We regard such objects (detected in I_c and z'-bands, but not in V-band) as candidates at $z \sim 5$, if they enter the selection window.

Among the 35,362 detected sources, 321 objects with $I_c \leq 25.5$ fall within this selection window. There are 11 objects with $I_c < 23.0$. Most of them lie close to the boundaries of our color selection criteria, and all of them are clearly visible in our V-band image. They have round shapes, suggesting that they are elliptical galaxies with old stellar population at intermediate redshift. They are also unusually luminous if they are star-forming galaxies located at $z \sim 5$ (absolute UV magnitude would be $\lesssim -22$). We regard them as the interlopers with peculiar colors and excluded them from our candidate list. In figure 3.1, we show V, I_c and z'-band images of the representative objects in our LBG candidates in an order of I_c magnitude.

3.1.3 Cross-identification with Galaxies at $z > 4$ in the HDF-N and Its Flanking Fields

We find six LBG candidates in the HDF-N region. The range of the I_c magnitude of these objects are from 24.6 to 25.4. One object HDF 4−625.0 is spectroscopically confirmed to be at a redshift of 4.58, and for three objects photometric redshifts are provided by [Fernández-Soto et al. 1999]. The appearances of these four objects with redshift information in the HDF-N drizzled images, as well as in the Suprime-Cam images, are shown in figure 3.2. Among the three objects for which photometric redshifts are given, two galaxies (HDF 3−238.0 and HDF 4−505.0) have estimated redshifts of 0.92 and 1.44 respectively. These objects are detected in B_{450}-band, so these would be interlopers. The other object HDF 3−153.0, which appears to be a single object in our ground-based image, is identified as two resolved objects by [Fernández-Soto et al. 1999]; one object has a redshift of 1.24 and the other 5.32. Since the latter object is 0.9 mag brighter than the former in I_{814}-band, the detection by our selection criteria is presumably attributed to the object at higher redshift. As we will describe in the next section, the fraction of interlopers at this magnitude range is expected to be around 40 to 50 %. Thus it is not surprising that half of the objects with redshift information seems to be interlopers. The remaining two objects lie close to the edges of the HDF-N and photometric redshift measurement is not performed on them. The WFPC2 and Suprime-Cam images of these two objects are shown in figure 3.3.

In the flanking fields of the HDF-N we find 12 LBG candidates. Two galaxies have been previously identified spectroscopically as objects at $z \sim 5$. They are J123649.2+621539 (ES1), a serendipitously detected object at $z = 5.19$ [Dawson et al. 2002], and B01−174, a broad-line AGN at $z = 5.186$ discovered in the Chandra Deep Field North region by [Barger et al. 2002]. The images of ES1 are shown in figure 3.1.

Vice versa, there are 7 galaxies in the HDF-N and its flanking fields, which have been spectroscopically identified as $4.4 < z < 5.5$ but are not included in our candidate list.[1] One object is located close to the edge of a CCD chip and the source detection was not executed there. Five galaxies are fainter than our magnitude limit or spatially unresolved with a nearby object in our image. The remaining one object is HDF 4−439.0, of which redshift is given as 4.54 by [Stern and Spinrad 1999]. The $V - I_c$ and $I_c - z'$

[1] There are three objects with a spectroscopic redshift larger than 5.5 in the HDF-N and its flanking fields. All of them are faint and not detected in our image. As it is described in the next section, incompleteness of our data gets larger for objects at $z \gtrsim 5.5$.

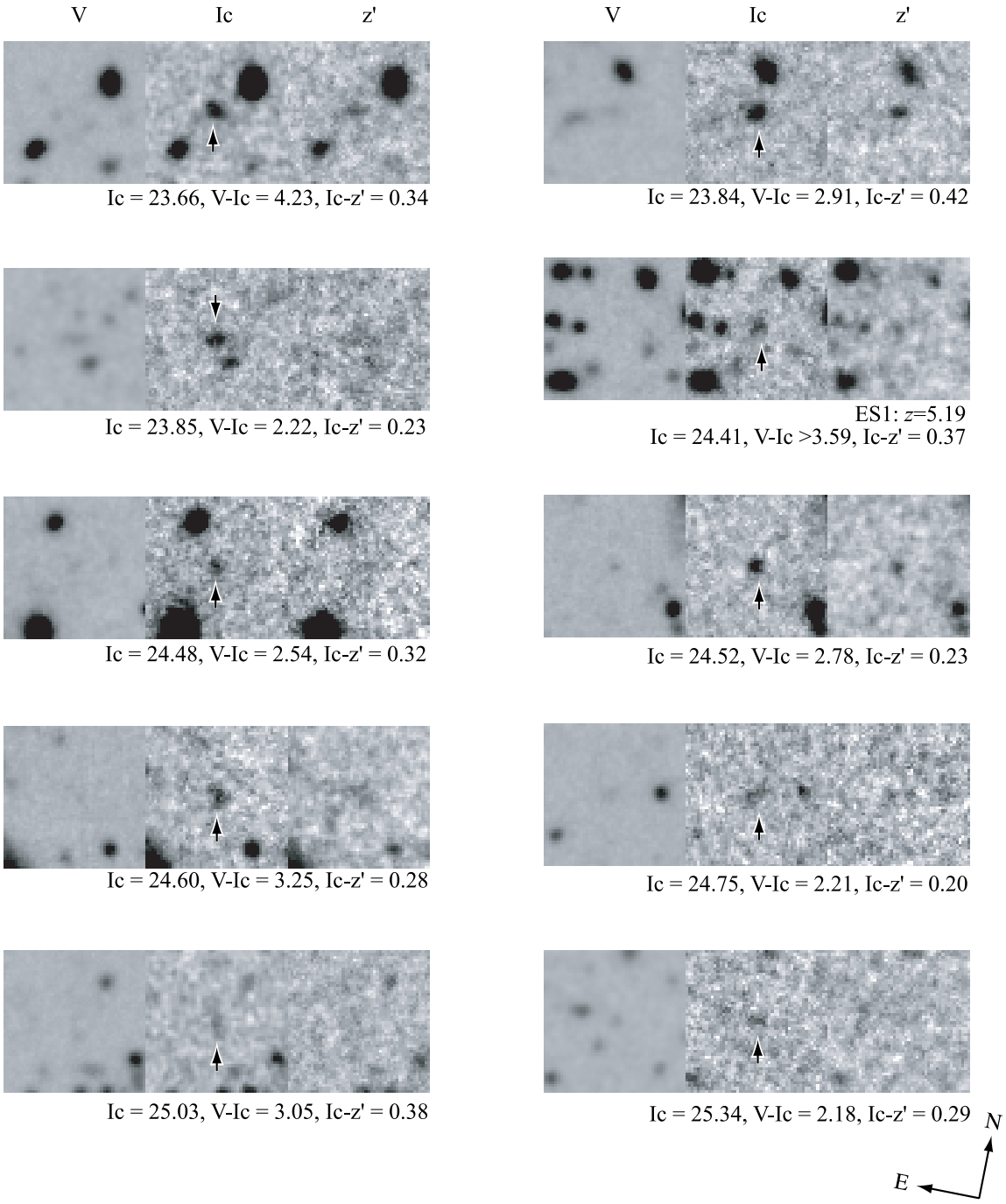

Figure 3.1: Images of the representative LBG candidates, in an order of I_c magnitude. From left to right, V, I_c and z'-band images are shown in each panel. The field of view is $10''$.

colors of the object are close to the boundary of our selection criteria, and we would fail to select the object probably due to the photometric error.

The detection rate of our survey for the objects with $I_{\rm AB}(814) \gtrsim 25.0$ with spectroscopic redshift between $4.4 < z < 5.5$ in the HDF-N and its flanking field is $\sim$1/3. It is consistent with the incompleteness estimated by the Monte Carlo simulations described in the next section.

3.2 Spatial Distribution

In figure 3.4 we show the spatial distribution of our LBG candidates projected to the sky in the equatorial coordinate. As a first glance one can easily notice that there is an inhomogeneity of the distribution of LBG candidates. There are some regions where LBG candidates "concentrate", and regions appear to be "voids" with a scale of 5 – 10 arcminutes. A 10 arcminute correspond to approximately 16 h^{-1} Mpc in comoving coordinate at $z = 5$, under the assumption of the cosmology with $\Omega_{\rm M} = 0.3$, $\Omega_\Lambda = 0.7$. We do not intend to further discuss the clustering properties of LBGs at $z \sim 5$ here. As it is described in the next chapter, there must be contamination of the objects with intermediate redshift, and the fraction of such interlopers would be ~ 50 % in the magnitude range $25.0 < I_c \leq 25.5$. Follow-up spectroscopy is essential to examine the three-dimensional distribution. Otherwise statistical treatment of incompleteness should be necessary (e.g., Giavalisco et al.; Ouchi et al.).

3.3 Size and Morphology

In regard to the effect of the merging event on the star formation activity of the LBGs, it is interesting that the HDF-N I_{814} image of HDF 4−625.0 at $z = 4.58$ shows the sign of merging or interaction (see the bottom panels in figure 3.2). If we can figure out the rate of mergers in our sample, we might be able to assess the effect of merging events on the star formation of the LBGs. Although our ground-based images have poor angular resolution and is not as deep as HDF-N HST/WFPC2 images, we try to examine the fraction of galaxies showing a sign of interaction with other galaxies among our LBG candidates. We count the number of objects which have multiple cores in I_c and z'-bands and are not seen or significantly faint in V-band among our LBG candidates with I_c magnitude between 24 and 25 (An example is the object with $I_c = 24.60$ in figure 3.1). Roughly 10 % of the LBG candidates show such feature. This fraction should, however, be regarded as a lower limit, since we cannot distinguish close encounters and mergers from a single object. The seeing condition of our observation ($\sim 1''$, corresponding to ~ 4.4 h^{-1} kpc for $z = 5.0$, $\Omega_{\rm M} = 0.3$ and $\Omega_\Lambda = 0.7$) is not suitable for the detailed analysis of the sizes and morphologies of the LBG candidates; about 40 % of the candidates have half light radius comparable to the seeing size.

3.4 Magnitude and Color Distribution

In figure 3.5, apparent I_c magnitudes against the color $(I_c - z')$ are plotted. A tendency that bright blue candidates are deficient is seen. Other any clear trends are not seen, though the photometric error is larger for faint objects ($\sim$0.45 mag in $25 < I_c < 25.5$). Figure 3.6 shows a distribution of $I - z'$ colors of the LBG candidates with $I_c \leq 25.0$ in our search. The $I_c - z'$ color of 0.07 mag corresponds to the bluest model LBG spectrum we adopted in section 2.1, which is regarded here as the extinction free template LBG spectrum. If the redder $I_c - z'$ colors originate in the internal extinction, we are able to derive a rough estimate of the extinction of each galaxy by comparing with the model spectra with different degree of extinction. In the upper abscissa of the figure, we indicate the $I_c - z'$ color of the model spectra of LBGs at $z = 5$ with $E(B - V) = 0.0$ to 0.4 assuming the extinction law by [Calzetti et al. 2000]. The distribution of $E(B - V)$ of the LBGs at $z \sim 3$ estimated by [Steidel et al. 1999] is also shown in figure 3.6 (dashed curve). The distribution of $E(B - V)$ based on the template fitting for rest-frame UV to optical SEDs of LBGs at $z \sim 3$ [Papovich et al. 2001] is broadly consistent with that of [Steidel et al. 1999]. Although the photometric errors for fainter objects in our candidates are large and a possible

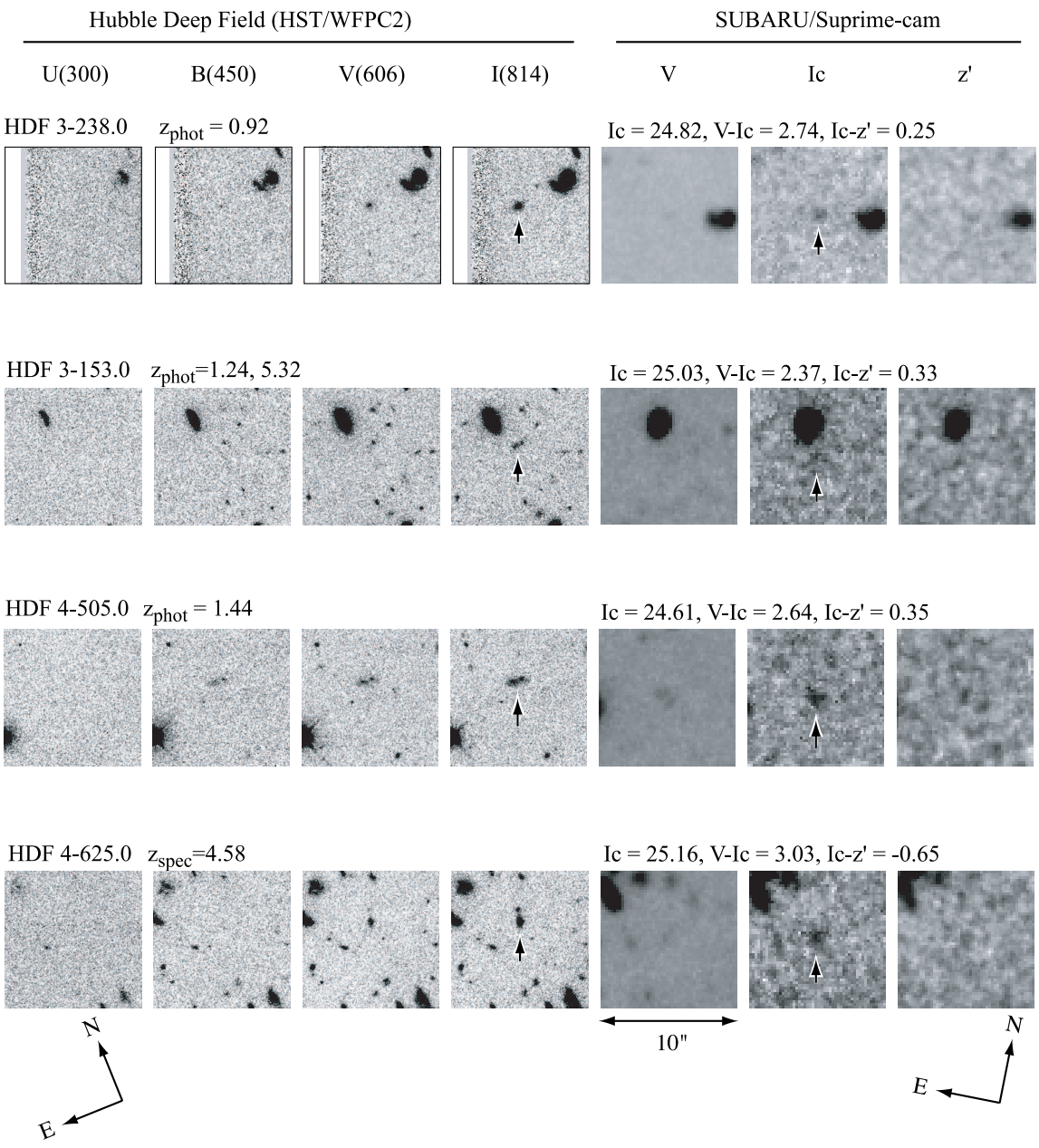

Figure 3.2: Images of four LBG candidates in the HDF-N region, of which redshifts (either spectroscopic or photometric) are available. The field of view is $10''$. Note that position angles of HDF/WFPC2 images and Suprime-Cam images are different, as shown in the bottom of the figure.

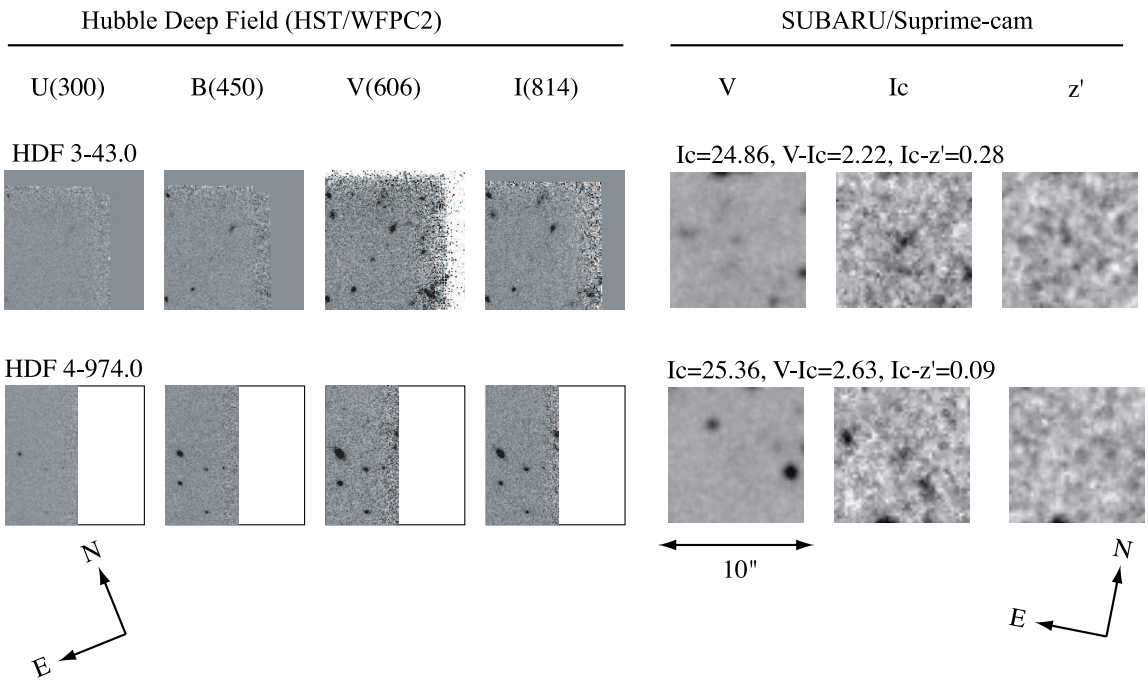

Figure 3.3: Same as figure 3.2, but for two LBG candidates in the HDF-N region, of which redshifts are not available.

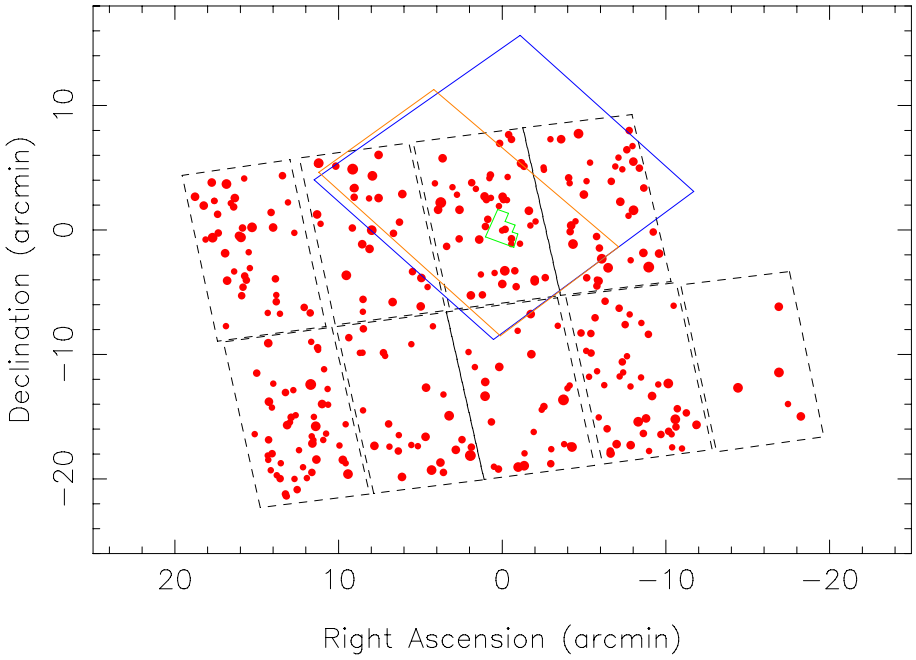

Figure 3.4: Spatial distribution of LBG candidates (solid circles). Size of symbols represent I_c magnitude of the object. The largest one is for $23.0 < I_c \leq 23.5$, and the smallest one is for $25.0 < I_c \leq 25.5$. The boxes with dashed line are boundaries of Suprime-Cam CCD chips. The coordinates are centered on the position of the HDF-N (RA(2000) = 12h36m49s.4, Dec(2000) = +62D12'58"). WFPC2 image area is shown with a green box. The blue and orange boxes stand for the field of the Chandra Deep Field-North [Brandt et al. 2001b] and the GOODS (Great Observatory Origin Deep Survey) [Dickinson et al. 2002], respectively.

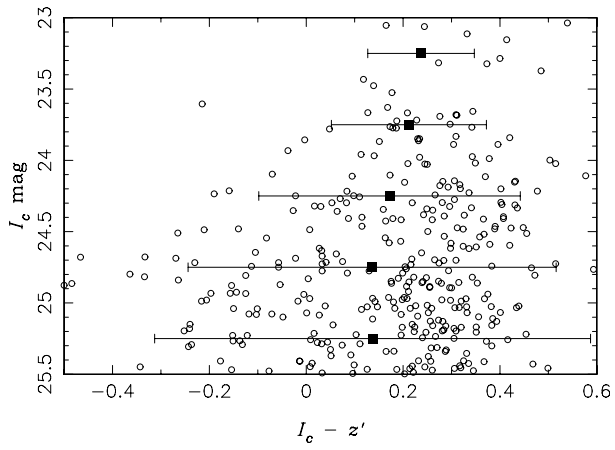

Figure 3.5: Apparent I_c magnitude against $I_c - z'$ color for LBG candidates at $z \sim 5$. Mean values of $I_c - z'$ colors in 0.5 I_c mag step are shown with filled squares. Each error bar represents the photometric error of the $I_c - z'$ color in each 0.5 magnitude bin.

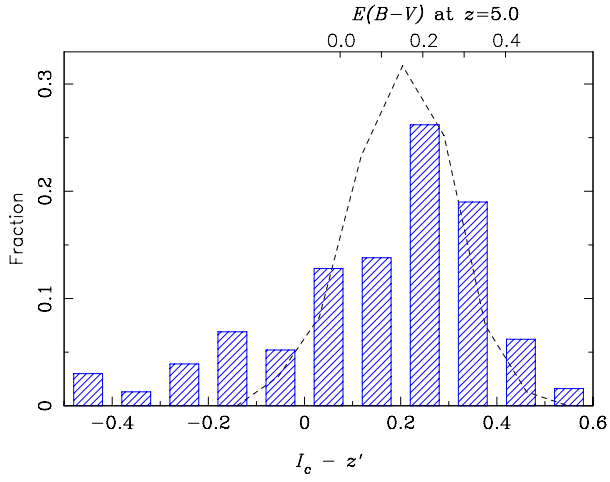

Figure 3.6: $I_c - z'$ color distribution of LBG candidates at $z \sim 5$. The objects with $I_c - z'$ colors less than -0.5 are included in the bin for the bluest color. The ticks at the upper horizontal axis indicate the expected $I_c - z'$ colors of a model galaxy at $z = 5$ with $E(B - V)$ from 0.0 to 0.4. See text for the details. The dashed line shows a distribution of $E(B - V)$ for LBGs at $z \sim 3$ by [Steidel et al. 1999].

contamination by the emission lines might disturb this distribution, the degree of the dust extinction for LBG candidates detected by our search seems to be similar to those at $z \sim 3$.

Chapter 4

The Luminosity Function of the LBGs at $z \sim 5$

In this chapter, we try to derive a luminosity function of LBGs at $z \sim 5$ using our LBG candidates. The redshifts of the candidates are not yet confirmed by spectroscopy except for a few objects. However, considering that the method works so efficiently at $z \sim 3$ and $z \sim 4$ and the color selection criteria adopted here is well examined thanks to a large redshift database based on deep spectroscopic and multi-waveband photometric observations in HDF-N and its flanking fields, we believe the catalog is reliable enough to discuss *statistical* nature of them. We would like to make follow-up spectroscopy in future, but it would take long years. Under these circumstances, constructing luminosity function and discussing its implication to cosmic star formation history statistically is opportune at this stage. In deriving the luminosity function of the LBGs at $z \sim 5$, we should consider the two important issues; contamination by interlopers and incompleteness of the sample. In the following procedure of this section we exclude the data in the CCD chip at the south-west corner with many bad columns; only five candidates are detected in the chip.

4.1 Correction for Contamination by Interlopers

In section 3.1 it has been described that our selection criteria are defined to be least contaminated by interlopers via redshift database of galaxies in the HDF-N and its flanking fields. While the galaxies in the HDF-N and its flanking fields are quite useful for the determination of the selection criteria, they are not suitable for the estimation of a number of interlopers contained in our LBG candidates, because the number of these galaxies with available redshift is only a few per cent of all the detected sources in our survey. Thus the estimation of the contamination rate based on the whole sample of detected objects in our catalog is necessary for the proper correction for interlopers.

There are some possible causes of contamination by interlopers other than the photometric errors: the first one is interlopers with colors which are intrinsically similar to LBGs at $z > 4.5$, and the second one is systematic errors due to the indirect z'-band calibration (section 2.3). The fact that there is no object at intermediate redshift for galaxies in the CFGRS and only two among 317 galaxies in the photometric redshift catalog of HDF-N by [Fernández-Soto et al. 1999] (see section 3.1 and figures 2.2b and 2.2c) would certify the validity of our selection criteria (equation (1) and (2) in section 3.1). This estimation of contamination by interlopers described below is based on this assumption. In regards to the systematic error due to z'-band calibration, it does not affect to our results, because we have defined our color selection criteria based on the colors of galaxies at the intermediate redshift in the HDF-N and its flanking fields. If $I_c - z'$ color distribution is shifted due to the systematic zero point shift in z'-band, the color selection criteria should also be shifted in the same direction. So we only consider photometric errors in quantifying the degree of contamination below.

The fraction of interlopers varies with their apparent magnitude, because the larger photometric errors in the measurement of fainter objects should increase the probability of their invasion into the $z \sim 5$ selection window even if their intrinsic color is the same as the brighter ones. Thus we should

estimate and correct the fraction of the interlopers at each magnitude bin. In order to accomplish this task, we employed a resampling (bootstrap) algorithm. First, we selected objects at the outside of the selection window in the $V - I_c$ and $I_c - z'$ color diagram from all of the detected objects. Then we divided them by their I_c magnitude with a 0.5 mag step. For each magnitude bin, we resampled objects randomly allowing the possibility of duplication. The number of objects included in a resampled group was the same as the number of objects in the magnitude bin. Then we assigned photometric errors to $V - I_c$ and $I_c - z'$ colors according to the observed I_c magnitude and color of each object; thus also according to V and z'-band magnitude. The error values in each band were based on the estimation by putting many artificial objects, and the obtained error values are consistent with those estimated from the background noise with $1''.6$ diameter (see section 2.3). The typical values for objects with colors close to the border of our color selection criteria were 0.07 mag and 0.11 mag for $V - I_c$ and $I_c - z'$ colors, respectively, for objects with $23.0 < I_c \leq 23.5$, and 0.43 mag and 0.45 mag for $V - I_c$ and $I_c - z'$ colors, respectively, for objects with $25.0 < I_c \leq 25.5$. The error assignment was made randomly under the assumption that photometric errors have a Gaussian distribution. We counted the number of objects of which modified colors are in the selection window. We ran this procedure 1,000 times for each magnitude bin and we regard the average of the numbers of objects that fall in the selection window as the estimated number of interlopers. We also performed the same procedure by adding objects which are placed inside of the selection window but are close to the boundary; their color differences from the boundary of the selection criteria are within the photometric errors in both $V - I_c$ and $I_c - z'$. By this test we intend to estimate a possible maximum number of interlopers. The number of objects within the window after adding the random error was roughly twice the number resulted in the first test (in which the objects at the outside of the selection window are used) over the all magnitude ranges. Since some (not all, but unknown) fraction of the objects within the selection window is considered to be interlopers, the first test should underestimate the number of interlopers, while the second test should overestimate it. We took the average of the results of these two tests as the expected number of interlopers. The variation of the number densities caused by this uncertainty in the estimation of the interlopers is ~ 10 – 30 % for all magnitude bins. We show the number of the interlopers thus obtained in table 4.1. The estimated fraction of interlopers gradually increases along with the magnitude, from 22 % at $23.0 < I_c < 23.5$ to 48 % for $25.0 < I_c < 25.5$. The result is consistent with the fact that no or only a few interlopers are seen for spectroscopic or photometric redshift catalog obtained in the HDF-N and its flanking fields (figure 2.2b and 2.2c), since the area of the HDF-N is smaller than our effective surveyed area by a factor of $\sim$ 100.

Subtraction of these numbers from the numbers of objects within the color selection window gives the expected numbers of objects at $z \sim 5$ if there is no contamination of noise. As described in section 2.4, the cross-identification of the sources with the HDF-N catalog shows that in the magnitude range $I_c \leq 24.5$ the sources are almost noise-free. In the fainter magnitude range, we have to multiply the expected number (difference of the values in columns 2 and 3 in table 4.1) by the fraction of the real objects among the total list of detected sources (1 minus the values in the fourth column in table 4.1), because the fraction of noises for the detected sources outside of the color selection window must be the same as that in the window. Accordingly, we obtain $N(m)$, the corrected number of objects at $z \sim 5$ in a magnitude range between $m \pm 0.25$.

4.2 Correction for Incompleteness

The other thing that we have to consider for the proper derivation of the luminosity function is the correction for the incompleteness of our survey. We should consider two aspects of incompleteness [Steidel et al. 1999]. One is the detection rate against the magnitude; the detection rate decreases with increasing magnitude, which is the usual detection incompleteness. The other one is the rate against the redshift and color; as seen in figure 2.2a, at a redshift range around 4 – 4.5, the detection rate should strongly depend on the color of an object. In addition, at the higher redshift (say $z > 5.5$), the location of the detected sources in figure 2.2 goes out of the window when they are fainter than the detection limit in V-band.

In order to correct these incompleteness, we ran Monte Carlo simulations. These Monte Carlo simu-

Table 4.1: The number of objects detected in our survey with colors expected for galaxies at $z \sim 5$, and corrections for interlopers, noise misidentification, and incompleteness.

Magnitude range (I_c) (1)	Detected Number (2)	Expected Number of Interlopers (3)	Noise Rate[$*$] (4)	$N(m)$ ((2)−(3))*(1−(4))
23.0 – 23.5	6	1.3 (22%)	0.0	4.7
23.5 – 24.0	25	6.6 (26%)	0.0	18.4
24.0 – 24.5	61	18.5 (30.3%)	0.0	42.5
24.5 – 25.0	91	33.9 (37.3%)	0.036	55.0
25.0 – 25.5	122	58.5 (48.0%)	0.172	52.6

$*$: Fraction of misidentification of noise as an object, estimated by the cross-identification with the HDF-N catalog.

lations enable us to calculate the "effective volume" of our survey [Steidel et al. 1999],

$$V_{\rm eff}(m) = \int dz p(m,z) dV/dz, \tag{4.1}$$

where $p(m,z)$ is a probability of finding an object with a magnitude of m at a redshift of z, which can be obtained as the average weighted over the distribution of SEDs of LBGs.

First we created sets of artificial objects with various magnitudes and various colors at various redshifts. The number of objects created in each set is 200. The magnitude range was taken from 23 mag to 25.5 mag with a 0.5 magnitude bin. Their angular sizes were adjusted so that the size distribution of the model objects resembles that of real objects at the same magnitude. Their $V - I_c$ and $I_c - z'$ colors of LBGs at $z = 4.0 - 6.0$ were calculated using the model spectra reproducing those of LBGs described in section 2.1. The redshift step was 0.1. We took objects with five different colors, which correspond to $E(B-V)$ of 0.0, 0.1, 0.2, 0.3, and 0.4 for each redshift and magnitude using the model SEDs. Thus we created $5 \times 20 \times 5 = 500$ sets of 200 artificial objects for each of 8 CCDs. Then we put these artificial objects into our V, I_c and z'-band images with a random spatial distribution, and performed the object detection in the same way as we did for real objects. Next we counted the number of detected objects which fell in our selection window for $z \sim 5$ objects. The fraction of the objects which satisfied our color selection criteria can be regarded as the probability of detecting an object with the magnitude and the color at the redshift. Weighted average of the probabilities are calculated using the $E(B-V)$ distribution of LBGs at $z \sim 3$ by [Steidel et al. 1999] within the range of $E(B-V) = 0.0$ – 0.4 (see dashed curve of Fig. 3.6). As it is described in section 3.3, $E(B-V)$ distribution of our LBG candidates is suggested to be similar to that by [Steidel et al. 1999]. The resulting probability $p(m,z)$ averaged over 8 CCD chips is shown in figure 4.1. The overall decrease in detection rate along the magnitude is clearly seen. At the lower redshift ($z = 4 - 4.5$), the detection rate decreases because of the cutoff of the selection window; the degree of the decline depends on the color and thus the color distribution of LBGs. At the higher redshift ($z = 5.2 - 5.6$), the detection rate decreases because the sources detected in I_c-band but not in V-band go out of the selection window at the fainter I_c magnitude and at the redder $I_c - z'$ color. The sum of the effective volumes of 8 CCD chips obtained for each magnitude range is summarized in table 4.2 for the two cosmological models. The variation of $p(m,z)$ among 8 CCD chips is not large; the variation of the $V_{\rm eff}$ obtained by equation (3) for each CCD is a few % for the bright ($23.0 < I_c \leq 24.0$) sources, and ~ 35 % for the faintest sources. We show in figure 4.2 the variance of detection rates among 8 CCD chips for objects with $23.0 < I_c \leq 23.5$, $24.0 < I_c \leq 24.5$ and $25.0 < I_c \leq 25.5$.

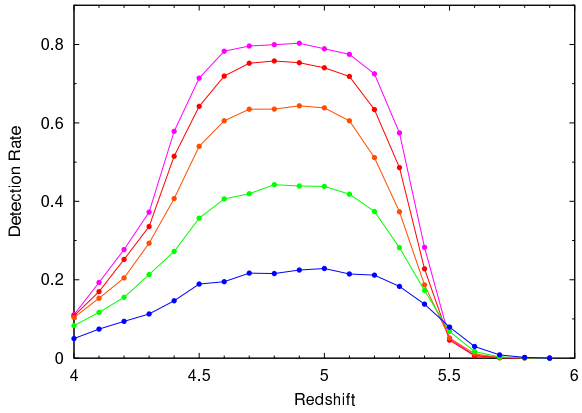

Figure 4.1: The detection rate $p(m, z)$ of the galaxies against the redshift of the objects estimated based on the Monte Carlo simulations. Each line indicates the detection rate for an I_c magnitude range of 23.0 – 23.5, 23.5 – 24.0, 24.0 – 24.5, 24.5 – 25.0 and 25.0 – 25.5 (from top to bottom).

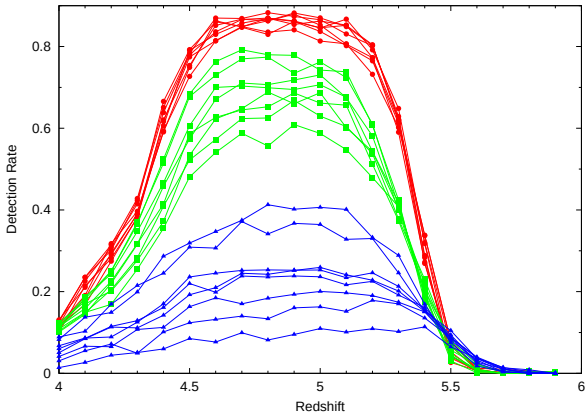

Figure 4.2: Chip-to-chip difference of the detection rate $p(m, z)$ of the galaxies. Red, green and blue lines show detection rates per CCD chip for objects with $23.0 < I_c \leq 23.5$, $24.0 < I_c \leq 24.5$ and $25.0 < I_c \leq 25.5$, respectively.

Table 4.2: Number densities of LBG candidates at $z \sim 5$.

Magnitude		$\Omega_{\rm M} = 0.3$, $\Omega_\Lambda = 0.7$		
range (I_c)	$n(m)$[$*$]	$M_{\rm UV}$(AB)[†] $- 5 \log h$	$V_{\rm eff}$[‡]	$\log \Phi(m)$[§]
23.0 – 23.5	0.82± 0.41	−22.1 – −21.6	741.32	−4.65
23.5 – 24.0	3.20± 0.93	−21.6 – −21.1	679.07	−4.03
24.0 – 24.5	7.39± 1.83	−21.1 – −20.6	565.47	−3.58
24.5 – 25.0	9.57± 2.10	−20.6 – −20.1	388.65	−3.31
25.0 – 25.5	9.14± 2.79	−20.1 – −19.6	204.31	−3.05

Magnitude		$\Omega_{\rm M} = 1.0$, $\Omega_\Lambda = 0.0$		
range (I_c)	$n(m)$[$*$]	$M_{\rm UV}$(AB)[†] $- 5 \log h$	$V_{\rm eff}$[‡]	$\log \Phi(m)$[§]
23.0 – 23.5	0.82± 0.41	−21.2 – −20.7	174.01	−4.02
23.5 – 24.0	3.20± 0.93	−20.7 – −20.2	159.40	−3.40
24.0 – 24.5	7.39± 1.83	−20.2 – −19.7	132.74	−2.95
24.5 – 25.0	9.57± 2.10	−19.7 – −19.2	91.21	−2.68
25.0 – 25.5	9.14± 2.79	−19.2 – −18.7	47.94	−2.42

$*$: Surface number density of LBG candidates in 10^{-2} arcmin^{-2} per 0.5 mag. These are derived by dividing $N(m)$ in table 4.1 by the effective surveyed area (575.0 arcmin^2).
†: Absolute magnitude in ABmag (I_c(AB) = I_c(Vega) + 0.45), calculated from I_c magnitude by assuming the redshift of 5.0 for all the objects.
‡: Effective volume of our survey in the unit of h^{-3} Mpc^3 arcmin^{-2}.
§: Number density of the $z \sim 5$ LBG candidates in the unit of h^3 mag^{-1} Mpc^{-3}.

4.3 Luminosity Function at $z \sim 5$

The information on the contamination of the interlopers and the incompleteness of our search described in the previous two subsections allow us to calculate the luminosity function of the Lyman break galaxies at $z \sim 5$ as,

$$\Phi(m) = N(m)/V_{\rm eff}(m), \tag{4.2}$$

where $N(m)$ is the number of objects in a magnitude bin of m corrected for the estimated contamination by interlopers and noise. The luminosity function thus derived is that at rest UV 1340 Å, which redshifts into the central wavelength of I_c-band (8060 Å) for a redshift of 5. In order to compare it with the luminosity functions at $z \sim 3$ and $z \sim 4$ obtained by [Steidel et al. 1999], we calculate absolute AB magnitudes at 1700 Å and derive the luminosity function at the wavelength, assuming a flat spectrum (in f_ν) which corresponds to $I_c - z'$ color of 0.1 mag in Vega magnitude system. Table 4.2 shows the number density of the LBG candidates in the 0.5 mag step corrected for the incompleteness and the contamination. The luminosity function of the $z \sim 5$ population is presented as red circles in figure 4.3. In deriving the luminosity function, we assume the redshift of 5.0 for all the LBG candidates to calculate their luminosity distance. If we use the weighted mean redshift of 4.8 derived from $p(m, z)$ (see figure 4.1) instead, the absolute magnitude becomes 0.10 mag fainter than that at $z = 5.0$. In order to show how much the corrections for contaminations and incompleteness affect the luminosity function, we show two alternative number densities with solid squares and triangles in figure 4.3. Solid squares represent the number density of LBGs at $z \sim 5$ in the case that the correction of contamination is skipped; i.e., all objects match with our color selection criteria are assumed to be genuinely at $z \sim 5$. Solid triangles indicate the number density assuming that the detection rate is 1.0 within a redshift range between 4.4 and 5.2 and otherwise 0 for all magnitude range instead of using the detection rates estimated by Monte Carlo simulation shown in figure 4.1. In figure 4.3 we also show the luminosity functions for $z \sim 3$ and 4 obtained by [Steidel et al. 1999] as open circles and open triangles. In deriving these luminosity functions, [Steidel et al. 1999] assume $\langle z \rangle = 3.04$ and $\langle z \rangle = 4.13$ respectively, according to the results of their spectroscopic observations.

There is no significant difference between the luminosity functions for $z \sim 3$, 4 and 5 in the bright

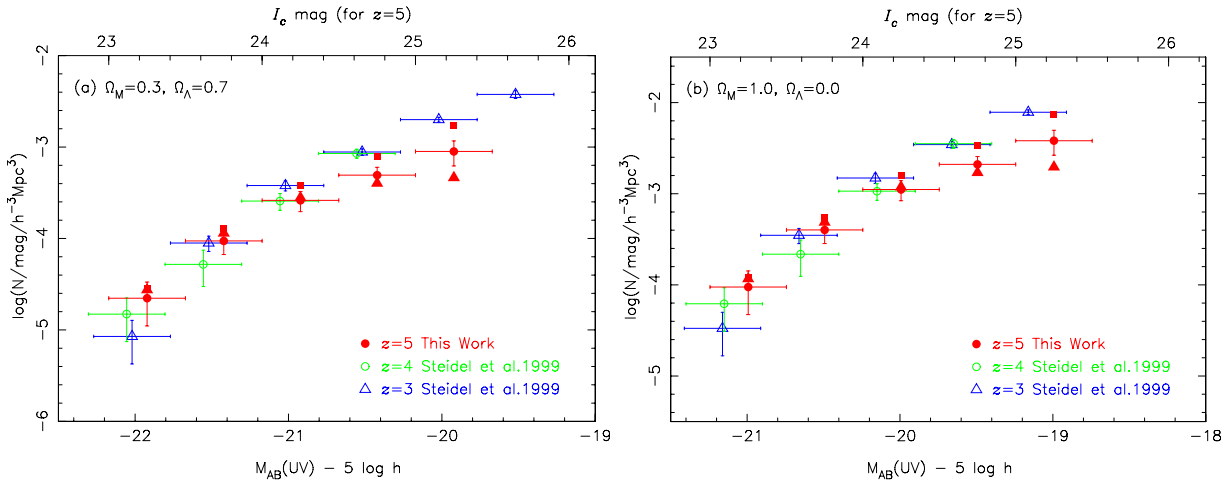

Figure 4.3: The luminosity function of the Lyman break galaxies at $z \sim 5$ (red). Assumed cosmology is $\Omega_{\rm M} = 0.3$ and $\Omega_\Lambda = 0.7$ for figure 4.3a and $\Omega_{\rm M} = 1.0$ and $\Omega_\Lambda = 0.0$ for figure 4.3b. The vertical error bars for our $z \sim 5$ data include errors in corrections for interlopers and incompleteness, as well as the statistical errors in the number of the candidates assuming the Poisson distribution. The assumed redshift is $z = 5.0$. The horizontal error bars indicate the magnitude step (0.5 mag) for all data points. The solid squares show the luminosity function without the correction of contamination, and the solid triangles are for a simple selection function which is 1.0 for a redshift range 4.4 to 5.2 and otherwise 0 regardless of magnitude. The open triangles and open circles represent the luminosity functions of LBGs at $\langle z \rangle = 3.04$ and $\langle z \rangle = 4.13$, respectively, taken from [Steidel et al. 1999]. The vertical error bars for them only show statistical errors.

part. Although the change of adopted cosmology makes a slight difference in the relative position of the data points, the general tendency remains in both figures. In the fainter part, there is a hint of the decrease of the number density at $z \sim 5$. It should be worth noting here that in figure 4.3, while the vertical error bars for our $z \sim 5$ data include errors in corrections for interlopers and incompleteness as well as the statistical errors in the number of the candidates assuming the Poisson distribution, the error bars for $z \sim 3$ and 4 by [Steidel et al. 1999] only include the statistical errors. Since the incompleteness of the $z \sim 3$ survey is reported to be comparable to or slightly better than ours [Steidel et al. 1999], if the uncertainty in the corrections for incompleteness and contamination of the interlopers are considered, the error bars for $z \sim 3$ data points should be larger than those appeared in figure 4.3. Thus within the current depth and uncertainties of the observed data it is hard to conclude whether the discrepancy between the number density for $z \sim 5$ and that for $z \sim 3$ at fainter part is real or not.

[Steidel et al. 1999] and [Adelberger and Steidel 2000] made the Schechter function fitting to the luminosity function of LBGs at $z \sim 3$ and derived a set of parameters $m^* = 24.54$, $\alpha = -1.57$ and $\phi^* = 4.4 \times 10^{-3}$ h^3 mag^{-1} Mpc^{-3} under the assumption $\Omega_M = 0.3$ and $\Omega_\Lambda = 0.7$. We made an error-weighted Schechter function fitting for our data for $z \sim 5$, and derived $m^* = 24.5$, $\alpha = -1.50$ and $\phi^* = 1.1 \times 10^{-3}$ h^3 mag^{-1} Mpc^{-3}. In figure 4.4 we show these two Schechter functions overplotted on the observed data points, as well as a UV luminosity function at the local universe derived by [Sullivan et al. 2000]. [Sullivan et al. 2000] used a sample of 433 galaxies with $0.0 < z \lesssim 0.4$, observed at 2000 Å.

[Meurer et al. 1999] suggest that the existence of the correlation between the rest-frame UV color and luminosity of the LBGs at $z \sim 3$; bright LBGs tend to be red. [Ouchi et al. 2002] report that the number density of LBGs at $z \sim 4$ shows the excess of red galaxies, which is qualitatively consistent with the result by [Meurer et al. 1999]. In order to see whether such correlation between the UV color and the luminosity exists in our sample, we divide it into two subsamples by their $I_c - z'$ colors (rest-frame 1340Å − 1520Å) at the median value of 0.21 mag, and show luminosity functions of them in figure 4.5. In the bright part, the number density of the red galaxies ($I_c - z' \geq 0.21$) is slightly larger than that of the blue galaxies. This trend can also be seen in figure 3.5. However, the correlation between the luminosity and the color is not as clear as in [Ouchi et al. 2002], who performed the same procedure for their LBG

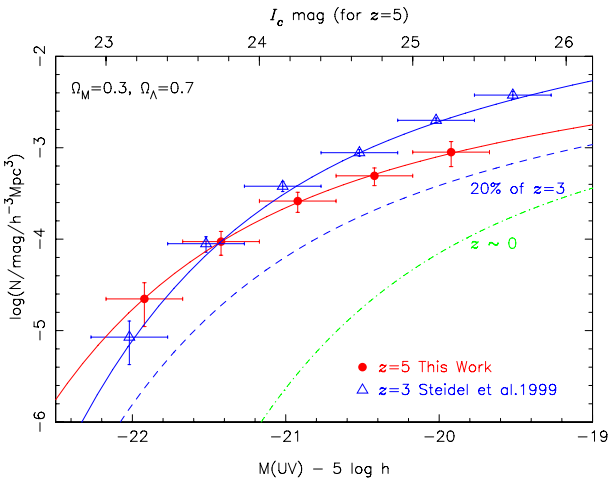

Figure 4.4: Same as figure 4.3a but only for LBGs at $z \sim 3$ and 5. Schechter functions fitted to the data are also shown. The dashed line indicates a Schechter function with 20% number density of LBGs at $z \sim 3$. Assumed cosmology is $\Omega_{\rm M} = 0.3$ and $\Omega_\Lambda = 0.7$. UV luminosity function at 2000Å in the local universe is also shown as a green dot-dashed line [Sullivan et al. 2000].

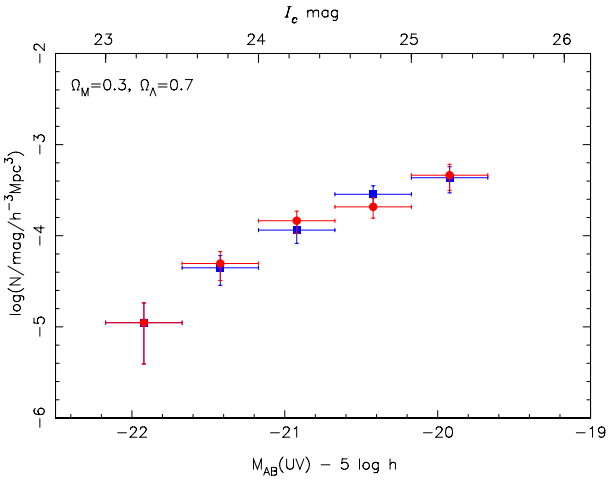

Figure 4.5: Luminosity functions of LBGs at $z \sim 5$ with red UV colors ($I_c - z' \geq 0.21$, red points) and blue colors ($I_c - z' < 0.21$, blue points).

candidates at $z \sim 4$ and found that red objects are more than two times abundant in the brighter part of the luminosity function. For objects with $I_c \leq 24.5$ in our sample, the number of red galaxies are ~ 1.14 times larger than that of blue galaxies. Although these results do not conflict with the results by [Meurer et al. 1999] and [Ouchi et al. 2002], the correlation of the UV color and luminosity in our $z \sim 5$ sample seems to be weaker than those at $z \sim 3$ and $z \sim 4$.

Chapter 5

Discussion

5.1 Star Formation History of an Individual LBG

Our results show that the luminosity function of LBGs at $z \sim 5$ is similar to those at $z \sim 3$ and at $z \sim 4$, though there may be a slight evolution in the faint part. Does this imply that the LBGs at $z \sim 5$ are the same LBGs at $z \sim 3$? Are they continuously forming stars during the period from $z \sim 5$ to $z \sim 3$ (~ 1 Gyr in our adopted Λ cosmology)? [Shapley et al. 2001] derived the ages of LBGs at $z \sim 3$ by the model SED fitting method assuming constant star formation. They found that the median age is 320 Myr and that many have ages less than 200 Myr and only 20% of them have ages larger than 1 Gyr. The fraction of the 20% depends slightly on the luminosity, but there is no clear tendency such as brighter objects have larger ages or vice versa. Therefore most of the LBGs at $z \sim 3$ were not yet forming stars at $z \sim 5$ and are not direct descendants of LBGs at $z \sim 5$, if we suppose the continuous star formation history for an individual object. In figure 4.5 we illustrate this with a Schechter function for 20% number density of LBGs at $z \sim 3$ as a dashed line, by simply assuming that each object has the continuous and constant star formation history with an age derived by [Shapley et al. 2001]. If we compare the number densities in the bright part (say $M_{\rm UV} - 5{\rm log}h \lesssim -21$), the number density for LBGs at $z \sim 5$ is close to that at $z \sim 3$ and the difference is distinct from the 20% line. The same situation is depicted by [Ferguson et al. 2002]. They also argue that an amount of star formation density at $z \sim 5$ contributed by the LBGs seen at $z \sim 3$ must be about ten times smaller than that at $z \sim 3$ for the continuous star formation history.

If the LBGs at $z \sim 3$ are not the direct descendants of LBGs at $z \sim 5$, did the LBGs at $z \sim 5$ stop star formation by $z \sim 3$? Do they fade out at $z \sim 3$? [Papovich et al. 2001] point out the absence of massive, non-star-forming galaxies in the HDF-N at $z \sim 3$. It may indicate that the descendants of LBGs at higher redshift which have stopped star formation and become fainter in UV by $z \sim 3$ are rare. Alternatively, the assumption of the constant star formation may not be appropriate; star formation may be sporadic. In this case, the ages derived by the SED fitting method would be taken to be those of the most recent starburst. [Papovich et al. 2001] test SED fitting using two-component models comprised of old and young stellar populations, and claim that two-component fitting generally gives smaller ages for the young population than the single-age models. The sporadic star formation and the short duty-cycle of the starburst would naturally explain the small ages of young stellar population and the existence of older stellar component as well as the similarity of the UV luminosity functions at $3 \lesssim z \lesssim 5$. Supposing the sporadic star formation history for individual galaxy seems to be reasonable, because the hierarchical clustering model generally implies merging process must occur for LBGs at high redshift. In this case, a burst of star formation may occur during a merging or a galaxy interaction. In fact, [Nagamine 2002] showed such sporadic star formation history for each galaxy takes place associated with a merging in a large-scale hydrodynamic simulation. He also presents a resultant V-band luminosity function at $z = 5$. We compare it with our result at UV, assuming a $UV - V$ color of the model template spectrum with a moderate reddening. Although the model luminosity function gives a good agreement with the number density of LBGs at the bright part, it shows a significant excess ($\sim$1 dex) in the fainter part. However, a color could depend on luminosity and this comparison seems to be premature; we need to compare our result with a model luminosity function directly derived at UV. Anyway such cosmological hydrodynamical simulations as well as semi-analytic approach are helpful for discussing star formation

processes of LBGs at high redshifts. We will return to this issue later.

5.2 Evolution of the UV Luminosity Density

5.2.1 UV Luminosity Density at $z \sim 5$

We can calculate the UV luminosity density at $z \sim 5$ by integrating the obtained luminosity function. In this calculation the integration is made in the magnitude ranges of $23.0 < I_c \leq 25.0$ and $23.0 < I_c \leq 25.5$. The former integration range is chosen to match with the limiting magnitude of $z \sim 4$ sample by [Steidel et al. 1999] in terms of absolute magnitude. Results are listed in table 5.1, together with those of $z \sim 3$ and $z \sim 4$ by [Steidel et al. 1999]. As it is expected from the shape of the luminosity function in particular at faint part, the resultant UV luminosity density at $z \sim 5$ is 0.56 – 0.69 times of that at $z \sim 3$ in the same absolute magnitude range, depending on the choice of cosmology and the integration range. The UV luminosity density seems to be getting smaller at higher redshift, though the difference between $z \sim 5$ and $z \sim 3$– 4 is comparable to the errors and we cannot rule out the possibility that the UV luminosities are almost constant at this redshift range. Madau et al. (1996, 1998) derived UV luminosity densities at $2 \lesssim z \lesssim 4$ using LBGs in the HDF-N. Their values are smaller than those by [Steidel et al. 1999] by a factor of 2–4. The search field for LBGs in the latter study is much larger than that of the former, and the discrepancy may originate in the small search volume in the HDF-N due to cosmic variance [Steidel et al. 1999]. [Casertano et al. 2000] also found 1.3 – 1.9 times higher UV luminosity density at $2 \lesssim z \lesssim 4$ in the HST/WFPC2 image of HDF-S as compared with that in the HDF-N.

In figure 5.1 we show the star formation density as a function of redshift. The assumed cosmology is $\Omega_{\rm M} = 0.3$ and $\Omega_\Lambda = 0.7$. The data point at $z \sim 5$ from our data and the points at $z \sim 3$ and 4 from [Steidel et al. 1999] are derived by the integration of the observed number densities for objects down to $M_{\rm UV} - 5{\rm log}h \lesssim -20$, as listed in table 5.1. For these data points at $z \gtrsim 3$, the UV luminosity density at 1500 Å is converted to star formation density using a conversion factor by [Madau et al. 1998], i.e., $SFR\ (M_\odot\ {\rm yr}^{-1}) = L_{\rm UV}\ ({\rm erg\ s^{-1}\ Hz^{-1}}) \times 1.25 \times 10^{-28}$. For $z \sim 5$ data point this gives SFR of 7.18×10^{-3} h $M_\odot$ yr^{-1} Mpc^{-3} (-2.14 in log scale) and 1.30×10^{-2} h $M_\odot$ yr^{-1} Mpc^{-3} (-1.88 in log scale) for Λ cosmology and Einstein-de Sitter cosmology, respectively. The data points for $z \sim 0.5$ – 2.0 are taken from [Connolly et al. 1997] which is based on the UV luminosity densities at rest-frame 2800 Å. For this wavelength we adopt a conversion factor $SFR\ (M_\odot\ {\rm yr}^{-1}) = L_{\rm UV}\ ({\rm erg\ s^{-1}\ Hz^{-1}}) \times 1.27 \times 10^{-28}$ also given by [Madau et al. 1998]. Originally their UV luminosity densities are given by integrating the Schechter UV luminosity function over the all luminosity range and calculation is made for Einstein-de Sitter universe. We adopt here a Schechter function with $\alpha = -1.3$, and for the consistency with data at $z \geq 3$, the integration of the UV luminosity function is made down to $M_{\rm UV} - 5{\rm log}h = -20$. The correction for different cosmological parameters is made following the prescription by [Somerville et al. 2001]. In figure 5.2 we also indicate the star formation density with a simple dust extinction correction as open symbols. In correcting dust extinction we follow [Steidel et al. 1999], who use the extinction curve by [Calzetti et al. 2000] and assume $E(B-V) = 0.15$ for all data points. As [Steidel et al. 1999] remark, the validity of such uniform correction is not clear, since the degree of extinction may be redshift dependent, and dust properties may change form time to time. As it is described in section 3.4, the $E(B-V)$ distribution estimated from $I_c - z'$ colors at $z \sim 5$ is similar to that of galaxies at $z \sim 3$ (figure 3.6), although the photometric error is large for faint objects. Thus the assumption that the degree of dust extinction is similar from $z \sim 3$ to 5 might not be inconsistent with our observed results for LBGs at $z \sim 5$, although there may be heavier dust extinction at $z \sim 1$ [Tresse et al. 2002].

[Steidel et al. 1999] also derived the UV densities at $z \sim 3$ and 4 by fitting Schechter function to the observed UV luminosity function and by integrating it down to 0.1 L^*, which corresponds to their faintest data point for $z \sim 3$ sample. For $z \sim 4$ sample, which is shallower than the $z \sim 3$ sample, they used the slope of Schechter function obtained for $z \sim 3$ sample ($\alpha = -1.6$). As it is described in section 4.3, the Schechter function fitting for our data for $z \sim 5$ LBG candidates gives $m^* = 24.54$, $\alpha = -1.57$ and $\phi^* = 4.4 \times 10^{-3}$ h^3 mag^{-1} Mpc^{-3} ($\Omega_M = 0.3$ and $\Omega_\Lambda = 0.7$). We show in table 5.1 the UV luminosity densities obtained by the integration of the fitted Schechter function with the integration range down to $0.1L^*$ as well as down to zero luminosity (i.e., all the luminosity range). The latter will

Table 5.1: UV luminosity densities.

	$\Omega_M = 0.3$, $\Omega_\Lambda = 0.7$ log ρ_{UV} [h erg s^{-1} Hz^{-1} Mpc^{-3}] [$*$]			
			Schechter function fitting	
redshift	$M_{UV} \lesssim -20.5$[†]	$M_{UV} \lesssim -20.0$[†]	$M_{UV} \leq M^* + 2.5$[‡]	$M_{UV} \leq \infty$[‡]
$z = 3$[§]	25.75±0.07	25.97±0.07	26.46	26.71
$z = 4$[§]	25.70±0.10 (89%)	–	26.36 (79%)	26.61 (79%)
$z = 5$	25.59±0.11 (69%)	25.76±0.16 (62%)	26.02 (36%)	26.27 (36%)

	$\Omega_M = 1.0$, $\Omega_\Lambda = 0.0$ log ρ_{UV} [h erg s^{-1} Hz^{-1} Mpc^{-3}] [$*$]			
			Schechter function fitting	
redshift	$M_{UV} \lesssim -19.5$[†]	$M_{UV} \lesssim -19.0$[†]	$M_{UV} \leq M^* + 2.5$[‡]	$M_{UV} \leq \infty$[‡]
$z = 3$[§]	26.05±0.07	26.27±0.07	26.71	26.96
$z = 4$[§]	25.96±0.10 (81%)	–	26.62 (81%)	26.87 (81%)
$z = 5$	25.85±0.11 (63%)	26.02±0.16 (56%)	26.28 (37%)	26.53 (37%)

$*$: Values shown in parentheses are percentage of the UV luminosity density relative to that at $z \sim 3$.
†: UV luminosity density obtained directly from the integration of the observed number densities.
‡: Estimated UV luminosity density by fitting to the Schechter function and integrated over the luminosity range as indicated. See text for the details.
§: [Steidel et al. 1999].

be used later for the comparison with the model predictions. Note that the integration of the luminosity function down to 0.1 L^* means the integration reaches to 26.9 mag in I_c-band, ∼1.4 mag fainter than our observational limit. The ratios of the UV luminosity densities at $z \sim 5$ and $z \sim 3$ obtained by these integrations are smaller than the ratios obtained by the direct sum of the luminosity function within our observational limit; the ratio drops to 0.36 for Λ cosmology. This is because in such extrapolated integration the contribution from fainter sources is dominant. We should keep in mind that, the number density of the LBGs with fainter magnitude is highly dependent on the estimated number of interlopers and on the effective volumes.

To examine a degree of uncertainty in deriving the UV luminosity density, we made a calculation of the luminosity function and the UV luminosity density using the smaller numbers of interlopers (the first test described in section 5.1). The resulting UV luminosity density is ∼ 1.2 times larger than those listed in table 5.1 (an increase of 0.08 in log scale). In addition, there is also an uncertainty in the estimate of the effective volume. From the chip-to-chip variation, the uncertainty of the effective volume for the whole survey area is estimated to be ∼ 10%. Taking these two uncertainties into account, the upper most possible UV luminosity density is estimated to be about 1.6 times (∼ 0.2 dex) larger than that shown in table 5.1. The value is comparable to the luminosity densities at $z \sim 3$ listed in table 5.1.

The UV luminosity density can be converted to the star formation density under the assumption that the UV continuum luminosity is proportional to the star formation rate (*SFR*). We adopt a conversion factor by [Madau et al. 1998], i.e., *SFR* ($M_\odot$ yr^{-1}) = L_{UV} (erg s^{-1} Hz^{-1}) ×1.25 × 10^{-28}. This gives *SFR* of 0.023 h $M_\odot$ yr^{-1} Mpc^{-3} (−1.63 in log scale) and 0.042 h $M_\odot$ yr^{-1} Mpc^{-3} (−1.37 in log scale) for Λ cosmology and Einstein-de Sitter cosmology, respectively, from the UV luminosity density derived by the integration over the all luminosity range. [Lanzetta et al. 2002] recently report their estimate of star formation density based on the photometric redshift data of the HDF-N and the Hubble Deep Field-South. They examine star formation rate intensity distribution function by taking care of the effects of cosmological surface brightness dimming. Integrating the function, they obtain the unobscured star formation rate density up to $z = 10$. In their lowest estimation ("scaling the break intensity" in their notation), the star formation rate density is roughly constant (but slightly rising up) from $z \sim 2$ to $z \sim 6$, as log(*SFR*) ∼ −1.2 to −0.9 h $M_\odot$ yr^{-1} Mpc^{-3} (with Einstein-de Sitter cosmology). These values are close to those obtained by [Steidel et al. 1999], but larger than our estimation at $z \sim 5$ derived from the

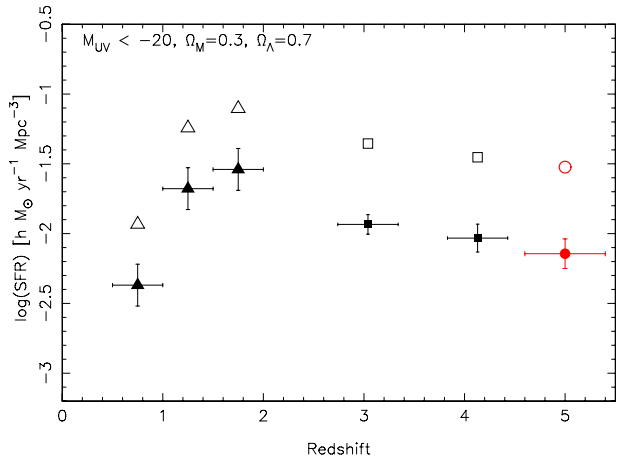

Figure 5.1: The star formation density as a function of redshift. Our data point for $z \sim 5$ LBGs are marked as a red filled circle. Our data and those by [Steidel et al. 1999] at $z \sim 3$ and 4 are derived by the integration of the luminosity function with absolute UV magnitude $M_{\rm UV} - 5 \log h \lesssim -20.0$ (see table 5.1). Three data points (shown in filled triangles) for $z \sim 0.5$ to 2.0 is from [Connolly et al. 1997], which are adjusted to $\Omega_{\rm M} = 0.3$, $\Omega_\Lambda = 0.7$ cosmology and to represent UV luminosities from objects with $M_{\rm UV} - 5 \log h \leq -20$. The conversion factors from UV luminosity (at rest-frame 1500Åfor $z \sim 3$ to 5 and 2800Åfor $z < 2$) to star formation density is from [Madau et al. 1998]. Filled symbols indicate values without correction for dust extinction. Dust extinction is corrected following the prescription by [Calzetti et al. 2000] with $E(B-V) = 0.15$ for all data points, and the values are shown with open symbols. Assumed cosmology is $\Omega_{\rm M} = 0.3$, $\Omega_\Lambda = 0.7$.

Schechter function fitting. However, it should be reminded that their method for deriving star formation rate density is different from that based on LBGs, and both our values and those by [Lanzetta et al. 2002] make extrapolation down to faint sources far beyond the observational limits.

5.2.2 Comparison with Model Predictions and Results of Numerical Simulations

It is interesting to make comparisons with results of semi-analytic models and of numerical simulations in terms of the cosmic star formation history and of the inference of plausible evolution process of LBGs. For the comparison of the cosmic star formation history, it would be desirable if the model predictions with an integration range compatible to the observational limit are available. Unfortunately we do not know such predictions among the published semi-analytic models and numerical simulations; they usually give the total star formation density. So we decided to estimate it by extrapolating the observational data. Further, for such comparison, the range of UV luminosity for integration should be uniform for all the observed data and model predictions. We should be cautious about such extrapolation, especially for the LBGs at high redshift, because the observed data only traces the bright part of the luminosity function. The UV luminosity densities of LBGs at $z \sim 3$ – 5 obtained by the Schechter function fitting are shown in table 5.1.

Another issue to be addressed for a proper comparison is the correction for dust extinction. The UV luminosity is highly sensitive for dust extinction, and it has been argued that substantial fraction of UV photons emitted from star forming regions of galaxies are absorbed. We adopt a simple and coarse correction for dust extinction following [Steidel et al. 1999]. They adopted Calzetti's extinction law with $E(B-V)$ of 0.15 for all data points at various redshifts. Since the $E(B-V)$ distribution estimated from $I_c - z'$ colors at $z \sim 5$ is similar to that of $z \sim 3$ galaxies (see section 3.3 and figure 3.6), this assumption would not be unreasonable for LBGs at $z \sim 5$. We note that this way of correction for the extinction is different from those by [Somerville et al. 2001] and [Ascasibar et al. 2002]. We show the resulting star formation densities uncorrected / corrected for the dust extinction in figure 5.2. In this figure the UV luminosity densities are integrated over the all luminosity range. If we use the integration range down to $0.1L^*$ instead, the data points at $z \sim 3$ to 5 go down by ∼0.25 dex, and those from the luminosity

function with shallower slope ($\alpha = -1.3$) such as by [Lilly et al. 1996] and [Connolly et al. 1997] decrease by ~ 0.10 dex.

In figure 5.2, we try to make a comparison of observed star formation density with those predicted by three different authors. A star formation history resulted from a numerical simulation based on the Cold Dark Matter cosmological scenario by [Ascasibar et al. 2002] is shown in figure 5.2(a). They employ a combination of N-body and hydrodynamical algorithm incorporating several feedback mechanisms such as photoionization by UV light from massive stars, gas heating and evaporation by supernovae. Their result shows a peak of star formation density at $z \sim 1$ and an overall constant star formation rate density at $z > 1$ with a slow decline. Their result gives a similar value of star formation density at $z \sim 5$ to our result, and the overall shape of star formation density as a function of redshift agrees with the observations. This rather constant star formation history during the period from $z = 2$ to 6 is also seen in a cosmological hydrodynamical simulation made by [Nagamine et al. 2001]. More recently, [Springel and Hernquist 2002] also report the result of their hydrodynamical numerical simulation. Their implementation of star formation is similar to that of [Ascasibar et al. 2002]. In addition to the feedback by supernovae, they incorporated the effect of galactic winds into their simulation. The star formation history as a result of their experiment exhibits a monotonic increase toward higher redshift by $z \sim 6$ and then decreases with z. The star formation rate density at $z \sim 5$ in their result is $\sim 0.1 M_{\odot}$ yr^{-1} Mpc^{-3} and it is comparable to the result by [Ascasibar et al. 2002].

We also show the predictions of two semi-analytic models by [Balland et al. 2003] and [Somerville et al. 2001] in figure 5.2(b) and (c). The model considered in [Balland et al. 2003] incorporates star formation induced by galaxy-galaxy interactions. They also consider the evolution of galaxy morphology in regards to the cumulative effect of energy exchange during interactions; a galaxy evolves from spiral to elliptical as total energy exchange gets larger than a threshold. The parameters for this energy exchange was determined according to the result of numerical simulation, and the thresholds dividing three morphological types (spiral, S0, elliptical) were adjusted so that fraction of three morphological types at the current universe was reproduced in their model. They yielded contributions from galaxies with different morphological types to the UV luminosity density, and they are shown in figure 5.2(b) with different curves. [Somerville et al. 2001] also examined the star formation history with the collision-induced star formation, as well as cases without it. In total they presented results with three star formation scenarios; They are "constant efficiency (CE) quiescent" model (red line in figure 5.2(c)), "accelerated quiescent" model (green line) and "collisional starburst" model (blue line). In the CE quiescent model, star formation is associated with the collapse or merging of dark matter halos, and the star formation rate is modeled to be proportional to a cold gas mass divided by a fixed time-scale. "Accelerated quiescent" model also assumes that the star formation rate is proportional to a gas mass, but time-scale of conversion from gas to stars is proportional to dynamical time of a galaxy. Because the density of collapsed dark matter haloes is higher at higher redshift, the dynamical time scale gets smaller as increasing redshift and as a result conversion from gas to stars becomes faster. The collisional starburst model incorporates starburst induced by galaxy-galaxy merger in addition to the CE quiescent star formation. For the galaxy-galaxy merger induced starburst, the efficiencies of the star formation are parameterized based on results by hydrodynamical simulations. The CE quiescent model cannot reproduce UV luminosity functions at $z = 3$ and 4 even if dust extinction is considered. Although the collisional starburst model produces abundance of luminous galaxies, if the dust extinction depending on luminosity is taken into account, the luminosity functions at $z = 3$ and 4 agree well with those obtained by [Steidel et al. 1999]. The CE quiescent model gives the lowest star formation rate density as seen in figure 5.2(c) (red curve). The disagreement between the model values and the observed data at the higher redshift is obvious. This quiescent model predicts that a star formation rate density at $z \sim 5$ is comparable to that at $z \sim 0$, which is not the case in our result. On the other hand, the predicted star formation density history based on the collisional starburst model in figure 5.2(b) and 5.2(c) (blue curve) is broadly consistent with the observed star formation rate density history.

[Somerville et al. 2001] pointed out that the satellite-central minor merger of galaxies, which is defined as the merging of the satellite galaxy with less than 25 % mass of the central galaxy, contributes most to the star formation rate density. These results obtained in semi-analytic models and cosmological hydrodynamical simulations suggest sporadic starburst associated with the merging processes of galaxies

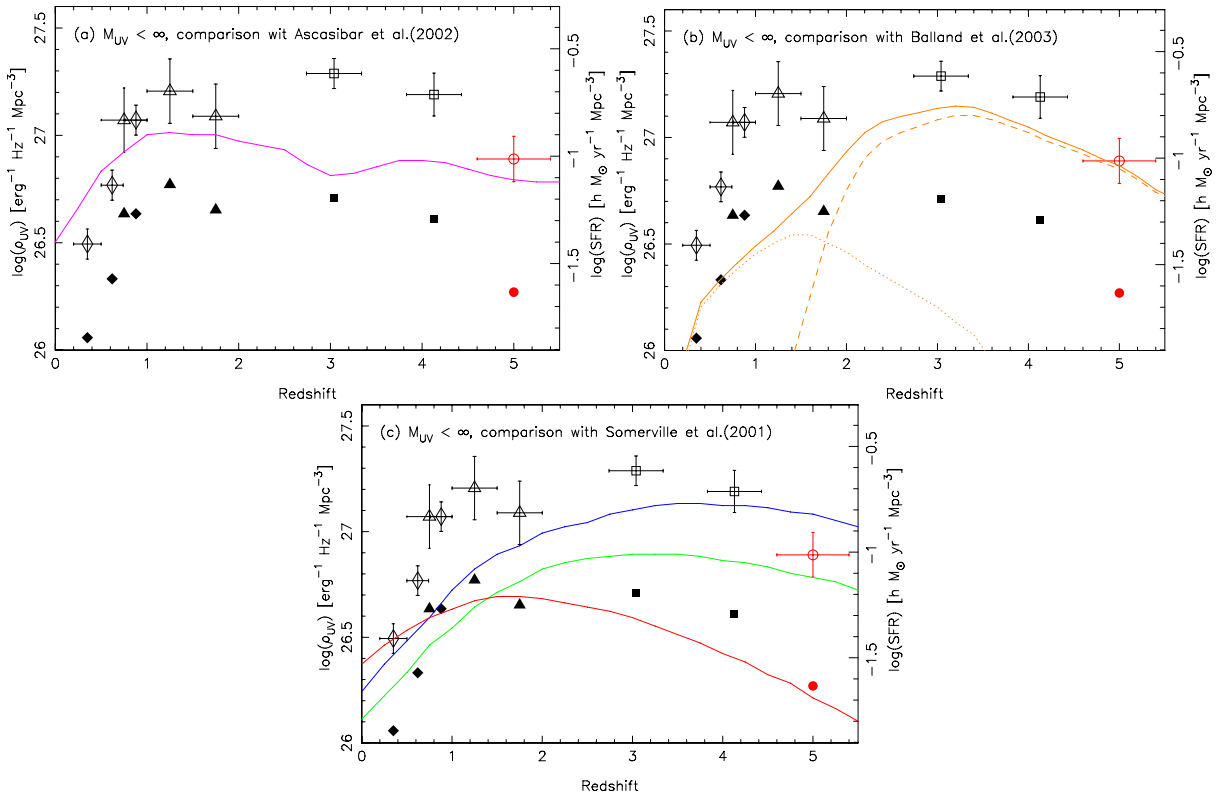

Figure 5.2: The star formation density as a function of redshift, derived by the conversion from the UV luminosity density as an integration of luminosity function over the all luminosity range. Assumed cosmology is $\Omega_M = 0.3$, $\Omega_\Lambda = 0.7$. Open symboles represent UV luminosity densities without extinction correction, and filled symbols show those after dust extinction correction, following the prescription by [Calzetti et al. 2000] with $E(B-V) = 0.15$ for all data points. Our data point for $z \sim 5$ LBGs are marked as a red circles. Previously published star formation densities at various redshift, all of them are estimated from the UV luminosity, are also indicated. [Lilly et al. 1996] (diamonds), [Connolly et al. 1997] (triangles) and [Steidel et al. 1999] (squares). **(a)**: Comparison with the result of a hydrodynamical numerical simulation executed by [Ascasibar et al. 2002]. **(b)**: Comparison with a prediction based on the semi-analytic models by [Balland et al. 2003]. The dotted line and dashed line is contributions from early type galaxies (E/S0) and from late type (spiral) galaxies, respectively. The solid line is a combination of these two populations. **(c)**: Comparison with predictions of semi-analytic models by [Somerville et al. 2001] (red: "constant quiescent" model, green: "accelerated quiescent" model, blue: "collisional burst" model).

dominates the star formation in the high redshift universe. If this is the case, it seems to be natural to suppose that most of LBGs at $z \sim 3-4$ are not genuinely quite young at the redshift, and they are descendants of LBGs at higher redshift. The absence of significant evolution in UV luminosity function from $z = 5$ to $z = 3$ may be accounted by integrating the sporadic star formation history for individual galaxy. Growth of stellar mass, dynamical mass, chemical abundance and so on from $z = 5$ to $z = 3$ may be able to be traced by examining properties of LBGs at $z \sim 5$ in detail. Follow-up spectroscopy and NIR imaging are necessary to reveal such evolution.

Star formation triggered by merging events would be helpful for explaining sporadic star formation history in an individual galaxy. As we have already described in section 3.3, although the seeing size of our image is too large to examine the morphology of LBG candidates, there are substantial fraction of objects with a sign of interaction. Space-based observation or imaging with adaptive optics for a large number of galaxies in our sample would be an interesting future task.

5.3 Contribution of Stellar Sources to the Ionizing Photon Density in the Intergalactic Medium

We briefly comment on the contribution of stellar sources to the hydrogen-ionizing radiation field at $z \sim 5$. Recently [Steidel et al. 2001] claimed that the escape fraction $f_{\rm esc}$, which represents the rate of Lyman continuum photons emitted outside from the galaxy, of the LBGs at $z \sim 3$ is significantly higher than the observational upper limit for star-forming galaxies in the local universe; it is comparable to or larger than 0.5 (but [Giallongo et al. 2002] made a deep spectroscopic observation for two LBGs and placed upper limit of $f_{\rm esc} < 0.16$). [Steidel et al. 2001] estimated the contribution of LBGs at $z \sim 3$ to the ionizing radiation field at 1 ryd to be $(1.2 \pm 0.3) \times 10^{26}$ h erg s^{-1} Hz^{-1} Mpc^{-3}, which is about 5 times larger than the contribution from quasars at the same redshift [Madau et al. 1999]. By the examination of absorption lines in QSOs, [Adelberger et al. 2003] found that HI is deficient at small distances from LBGs, partly due to the ionizing radiations from star forming region in LBGs (they argued that the apparent lack of HI cannot be explained merely by the ionizing radiation from LBGs, and pointed out that galactic superwinds from LBGs might be responsible for it). If the rapid decrease of quasar number density at $z > 3$ ([Fan et al. 2001] and references therein) is real, the number of ionizing photons radiated from quasars should strongly decline at higher redshift. [Madau et al. 1999] estimated it drops by a factor of $\sim$2 from $z = 3$ to $z = 5$. Provided that the escape fraction of LBGs at $z \sim 5$ is as large as 0.5, our estimate of the UV luminosity density at $z \sim 5$ implies the ionizing photons originated from star forming galaxies are $\sim$4 to 6 times larger than those from quasars at the redshift. In figure 5.3 we show a comparison of emission rates of ionizing photons from QSOs and star-forming galaxies at $z \sim 3$ and 5, based on the discussion made by [Madau et al. 1999]. This further suggests that the source of the UV photons which reionized the Universe at sometime of $z > 5$ is dominated by stellar origin. It is also interesting that, the ionizing photons from LBGs is comparable to the number of photons needed to fully ionize a universe considered in [Madau et al. 1999] (Einstein-de Sitter universe with a clumping factor of 30 and the baryon fraction $\Omega_b h^2$=0.02). However, this coincidence is based on the quite uncertain factors such as the quasar number density, the escape fraction of ionizing photons, and the clumpiness of the hydrogen gas in the early universe. A deep observation of the rest-frame far-UV wavelengths of LBGs is one of the indispensable subjects needed to clarify the nature of the ionizing radiation field at $z > 3$.

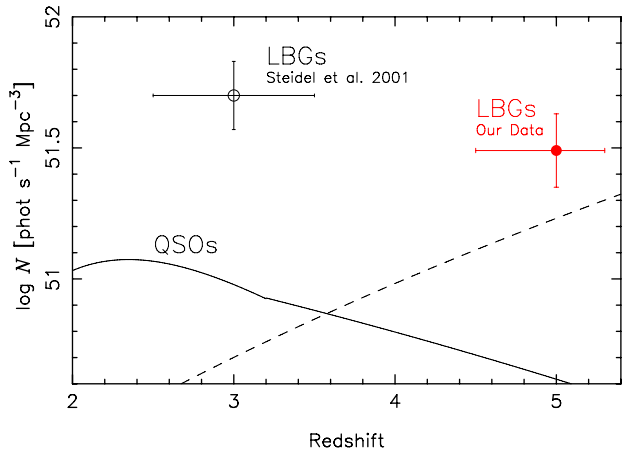

Figure 5.3: Emission rates of Lyman continuum photons from QSOs and star-forming galaxies. A solid line indicate comoving emission rate of ionizing photons from QSOs [Madau et al. 1999], estimated from the luminosity function of QSOs at high redshift. Open circle shows the emission rate from LBGs at $z \sim 3$ by [Steidel et al. 2001], assuming that half of the ionizing photons escape from galaxies to inter galactic space. Solid circle is a estimate of a contribution from LBGs to the radiation field at $z \sim 5$. This estimate is based on the comparison of the UV luminosity density at $z \sim 3$ and 5. The escape fraction of ionizing photon is assumed to be same as $z \sim 3$. A dashed line represents a emission rate of ionizing photons needed to fully ionize the hydrogen in the Universe with a clumping factor of 30 and the baryon fraction $\Omega_b h^2$=0.02 [Madau et al. 1999]. The assumed cosmology here is Einstein-de Sitter Universe ($\Omega_{\rm M} = 1.0$, $\Omega_\Lambda = 0.0$, $q_0 = 0.5$).

Chapter 6

Summary and Future Prospects

6.1 Summary

We have presented the results of a search for Lyman break galaxies at the redshift range between 4.4 and 5.3 in the field including the HDF-North with Suprime-Cam attached to Subaru telescope. Databases for galaxies in the HDF-N and its flanking fields enable us to find out the color selection criteria with least foreground contamination. Within the surveyed area of 618.6 arcmin^2 we have found 96 LBG candidates with $23.0 < I_c \leq 24.5$ mag, and 310 candidates with $I_c \leq 25.5$ mag. There is a hint of the deficiency of bright blue galaxies, although it is not as clear as suggested for LBGs at $z \sim 3$ to 4.

The contamination of objects at intermediate redshifts is estimated employing the resampling algorithm. The fraction of contamination amounts to ∼20% at bright part of the sample and ∼50% at the faintest magnitude range. We have also performed Monte Carlo simulations for the evaluation of the incompleteness of the survey. The completeness is estimated as a function of the magnitude and the redshift of an object; in the redshift range of $4.5 \lesssim z \lesssim 5.0$, it is ∼80% in the bright part of the sample and ∼20% in the faintest magnitude range. Using these corrections, we derive the luminosity function of LBGs at $z \sim 5$ statistically in the absolute UV magnitude range from -23.0 to -20.5 (with $\Omega_{\rm M} = 0.3$, $\Omega_\Lambda = 0.7$, $h_0 = 0.65$). No significant difference is seen between the luminosity function of LBGs at $z \sim 5$ and those at $z \sim 3$ and 4 obtained by [Steidel et al. 1999], though there might be a decrease of the number density at the fainter magnitude. We have compared the UV luminosity density at the redshift 5 to those at $z \sim 3$ and 4. If we adopt the direct sum of the luminosity function within our observational limit, the star formation density decreases to 56–69% of that at $z \sim 3$ estimated by [Steidel et al. 1999]. This decrease in UV luminosity density at $z \sim 5$ compared to $z \sim 3$ is due to the smaller number density of faint galaxies at $z \sim 5$. We cannot rule out the possibility that the UV luminosity density is almost constant at $z \gtrsim 3$, if we take account for the larger uncertainty in the faint part of the luminosity function. If we fit the Schechter function to the luminosity function and make an integration down to the fainter magnitude, the UV luminosity density at $z \sim 5$ is estimated to be ∼36% of that at $z \sim 3$. The star formation density at $z \sim 5$, derived by a simple conversion from the UV luminosity density, is estimated to be 0.023 h $M_\odot$ yr^{-1} Mpc^{-3}.

We have discussed on a plausible evolutionary scenario of LBGs based on our results. The similarity of the luminosity functions at redshifts 5 to 3 implies that most of the LBGs at $z \sim 5$ should have faded out at $z \sim 3$ and the LBGs at $z \sim 5$ are different galaxies from those seen at $z \sim 3$, if we take face values for ages of the LBGs at $z \sim 3$ obtained by the SED fitting in which a continuous star formation in an individual galaxy is assumed. However, if the star formation in LBGs is sporadic, the similarity of the luminosity function at $z \sim 3$ and 5 would be naturally explained. Such sporadic star formation has been suggested by hydrodynamical simulations and semi-analytic models with collisional starbursts, and the trend of the cosmic star formation history predicted by these studies resembles to that estimated from an integration of the UV luminosity density within the observational limit.

6.2 Future Prospects

In this last section, we describe several planned observations and analyses as the extension of this work.

6.2.1 Optical Spectroscopy and Imaging

The results presented here on the luminosity function and the UV luminosity density at $z \sim 5$ are based only on the imaging observation, and statistical treatment of the effects of the contamination by objects at intermediate redshift and the incompleteness of the survey was made. It is obvious that spectroscopic observations for LBG candidates are quite essential to confirm the validity of the selection criteria and estimation of the contamination based on resampling algorithm. It is also required to examine the three-dimensional distribution of the LBGs, since objects detected by the Lyman break method have relatively wide range of redshift distribution (see fig 4.1).

The first optical spectroscopic observation using FOCAS attached to the Subaru telescope is scheduled in February 2003. In this observation we aim to observe the brighter ($I_c < 24.5$) LBG candidates and to detect the Lyman α emission lines or Lyman break. The spectroscopic observation for fainter objects in our sample is not easy for 8-m class telescopes. For example for an object with $I_c \approx 25.5$ detection of continuum should require about 11 on-source exposure (Subaru/FOCAS, 150 lines/mm grating with S058 filter, S/N=5; it increases to 48 hours if we use 300R grating). Thus observing with wide-field multi-object spectrograph is quite important for achieving good survey efficiency.

For the improvement of statistical accuracy, increasing the number of objects in our sample with survey of other fields is a promising way. We have already started the survey with the same V, I_c and z'-bands filter sets in the field J0053+1234 using Suprime-Cam. This field is at a high galactic latitude ($b \sim -50°$) and low galactic extinction ($A_V = 0.13$). This field has been selected as the target of the extensive spectroscopic survey of faint galaxies executed by Caltech group ([Cohen et al. 1996]; [Cohen et al. 1999a]; [Cohen et al. 1999b]; [Hogg et al. 2000]). They provide positions, photometries and redshift information for 163 galaxies in this field. The limiting magnitude of spectroscopic data is $K < 20$ mag or $R < 23.5$ mag, and the median of obtained redshifts is ~ 1.0. In addition, [Steidel et al. 1999] made a search for LBGs at $z \sim 4$ in this region and published spectroscopic redshifts of 14 galaxies at $z \sim 4$. This abundance of redshift data in this field is quite essential for executing LBG search at high redshift; foreground contamination in this field can be mitigated as much as possible without invoking very time consuming spectroscopy. The excellent visibility of the J0053+1234 field compared to the HDF-N is a great advantage of this field in the technical aspect. We plan to accomplish the survey of this field in the year 2003 and increase the number of LBG candidates more than double.

6.2.2 Imaging at Near-infrared and Longer Wavelength. I. Imaging for LBG candidates at $z \sim 5$

One of the critical values indispensable to clarify the star formation in LBGs is the degree of dust extinction. Since UV photons are quite easily absorbed by dust, the estimation of UV luminosity highly depends on the degree of extinction. In section 3.4 we see that the reddening for LBGs at $z \sim 5$ estimated from the UV slope ($I_c - z'$ color) seems to be not so different from that for LBGs at $z \sim 3$ (figure 3.6). Although UV slope has been suggested to be a fairly good tracer of dust extinction (e.g., [Pettini et al. 2001]; [Seibert et al. 2002]), it is uncertain in the faint magnitude range due to the photometric error. The situation should become much better if we add the flux density and longer wavelength. That is a motivation for executing a near-infrared imaging of LBG candidates.

The improvement in the accuracy of determining the degree of dust extinction and the star formation history in individual galaxy expected by the addition of near-infrared data is schematically illustrated in 6.1. The lines represent the evolutionary sequences of galaxies calculated by a population synthesis code (PEGASE; [Fioc and Rocca-Volmerange(1997]). We consider three types of evolutionary stages of galaxies; a) on-going starburst, b) post-starburst, and c) passive evolution after an initial starburst. Lines with square symbols represents galaxies with on-going starburst. The lines with triangles are for galaxies at 50 Myr after a starburst with 200 Myr duration. And the lines with circles are for galaxies with 500 Myr age, whose stars have been generated instantaneously at formation epoch, and then stars in the galaxy evolve passively. Solid lines are for objects with a modest dust extinction ($E(B-V) = 0.2$), and dashed lines are for those without dust extinction. For all calculations in this figure we adopt an initial metallicity as $0.5Z_\odot$. The galaxies at different evolutionary stages are clearly separated in this figure. In $V - I_c$ versus $I_c - z'$ two-color diagram, these model galaxies lie within ~ 0.5mag in $I_c - z'$,

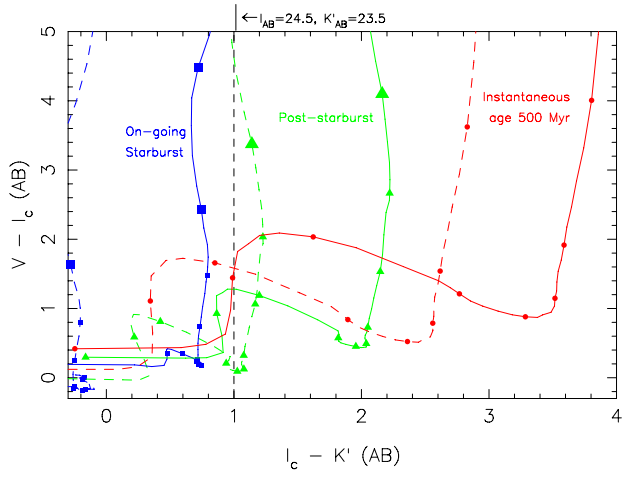

Figure 6.1: $I_c - K'$ versus $V - I_c$ diagram for model galaxies. Lines with symbols represent tracks of colors for model galaxies. Lines with squares, triangles and circles refer to a galaxy with on-going starburst, post-starburst (50 Myr after burst) and passively evolving galaxy after an initial instantaneous starburst (500 Myr age), respectively. The solid lines refer to a modest dust extinction ($E(B-V) = 0.2$, [Calzetti et al. 2000]), and dashed lines are for galaxies without dust extinction.

and it is practically impossible to discriminate one from others. In addition, we can estimate the amount of dust extinction much reliably than using UV slope (i.e., $I_c - z'$ color). In this figure metallicity of initial gas is fixed to 0.5 $Z_\odot$. In galaxies dominated by young stellar population, i.e., galaxies with on-going starburst or those at post-starburst phase, the effect of metallicity of the ISM on galaxy colors is negligible. According to our calculation using PEGASE, the difference of $I_c - K'$ color between a galaxy with initial metallicity 0.5 $Z_\odot$ and a galaxy with 0.1 $Z_\odot$ or 1.0 $Z_\odot$ is at most $\sim$0.1 mag for galaxies with on-going starburst or at post-starburst phase. Thus the estimation of the evolutionary stage and dust extinction are not seriously affected by the uncertainty in metallicity.

To obtain the wide range of SEDs, especially the flux density at the wavelength range longer than 4000Å, is needed to make a comparison with stellar population synthesis models, which has been proved to be a powerful tool for examining the star formation history and stellar mass for LBGs at $z \sim 3$(e.g., [Shapley et al. 2001]; [Papovich et al. 2001]). In this sense the LBGs found by us are good targets of the forthcoming space-based facilities, such as SIRTF and JWST (NGST), which have a capability of deep observation at $\gtrsim 3\mu$m.

6.2.3 Imaging at Near-infrared and Longer Wavelength. II. Application of Lyman Break Method to Galaxies at $z > 5.5$

The imaging at near-infrared wavebands is also essential for the search of galaxies at redshift larger than 5. At redshift of 5.5, the Lyman α emission line shifts to 7900 Å, and objects further than that redshift get dimmer in I-band. As it has been already mentioned by [Dickinson 2000], in order to discriminate such I-dropout high-z objects from galaxies with old stellar population at intermediate redshift we need near-infrared imaging data.

In order to assess a survey depth required to construct a sample with statistically meaningful number of galaxies at $z > 5.5$, we make a calculation of $I_c - z'$ and $z' - J$ colors for galaxies at various redshift. We made a model spectrum of star-forming galaxy using PEGASE. For simplicity the star formation history is assumed to be constant star formation rate and has an age of 100 Myr. In figure 6.2 we show a color track of the model galaxy with three types of dust extinction ($E(B-V) = 0.0$, 0.2, 0.4), as well as those for old elliptical galaxies and spiral galaxies. No evolution is considered in all models. It is seen that this set of filters are suited for the selection of galaxies at a redshift range roughly between 5.6 and 6.2. The number of galaxies expected to be detected by this way is estimated to be 0.13 per square arcmin for limiting magnitude of z'(AB)=25.5, if there is no evolution of the luminosity function from

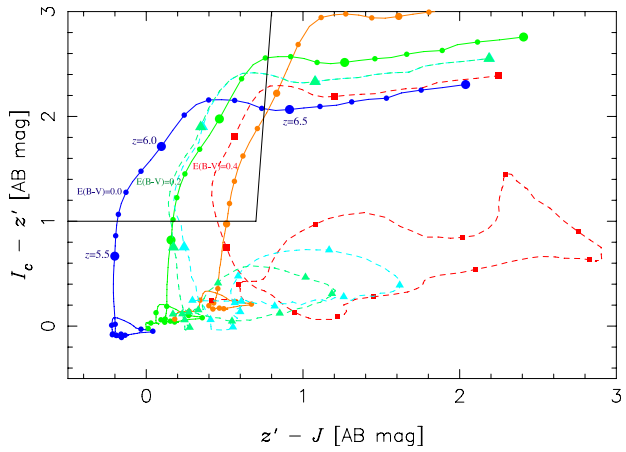

Figure 6.2: $I_c - z'$ and $z' - J$ two-color diagram. Solid lines represents color tracks of star-forming model galaxies at $0 \leq z \leq 7$, with no dust extinction (blue line), $E(B-V) = 0.2$ (green line) and $E(B-V) = 0.4$ (red line). The red dashed track is for a model galaxy with old stellar component (base on the population synthesis code developed by [Kodama and Arimoto 1997]). The colors calculated from model galaxy spectra by [Coleman et al. 1980] for Sbc and Scd galaxies are shown with a green and a cyan line, respectively. The symbols are drawn at a redshift step of 0.1. In computing colors we take into account of a dust extinction according to a prescription by [Calzetti et al. 2000], as well as absorption by intervening neutral hydrogen based on [Madau 1995]. The box enclosed by a black line indicates a color selection criteria for LBGs at $5.6 < z < 6.2$.

$z \sim 5$ to 6. The wide-field near-infrared imagers currently planned to be installed on the large telescopes would provide the opportunity of searches for objects at $z > 5.5$, and we may witness the first emergence of star forming galaxies in the universe.

REFERENCES

[Adelberger and Steidel 2000] Adelberger, K. L., & Steidel, C. C., 2000, ApJ, 544, 218

[Adelberger et al. 2003] Adelberger, K. L., Steidel, C. C., Shapley, A. E., & Pettini, M., 2003, ApJ in press (preprint: astro-ph/0210314)

[Ascasibar et al. 2002] Ascasibar, Y., Yepes, G., Gottlöber, S., & Müller, V., 2002, A & A, 387, 396

[Balland et al. 2003] Balland, C., Devriendt J. E. G., & Silk J., 2003, submitted to MNRAS (preprint: astro-ph/0210030)

[Barger et al. 1999] Barger, A. J., Cowie, L. L., Smail, I., Ivison, R. J., Blain, A. W., Kneib, J.-P., 1999, AJ, 117, 2656

[Barger et al. 2002] Barger, A. J., Cowie, L. L., Brandt, W. N., Capak, P., Garmire, G. P., Hornschemeier, A. E., Steffen, A. T., & Wehner, E. H., 2002, AJ, 124, 1839

[Bertin and Arnouts 1996] Bertin, E., & Arnouts, S., 1996, A & AS, 117, 393

[Baugh et al. 1998] Baugh, C. M., Cole, S., Frenk, C. S., & Lacey, C. G., 1998, ApJ, 498, 504

[Becker et al. 2001] Becker, R. H., Fan, X., White, R. L., Strauss, M. A., Narayanan, V. K., Lupton, R. H., Gunn, J. E., Annis, J., et al., 2001, AJ, 122, 2850

[Blain et al. 1999] Blain, A. W., Smail, I., Ivison, R. J., & Kneib, J.-P., 1999, MNRAS, 302, 632

[Brandt et al. 2001a] Brandt, W. N., Hornschemeier, A. E., Schneider, D. P., Alexander, D. M., Bauer, F. E., Garmire, G. P., & Vignali, C., 2001a, ApJ 558, L5

[Brandt et al. 2001b] Brandt, W. N., Hornschemeier, A. E., Alexander, D. M., Garmire, G. P., Schneider, D. P., Broos, P. S., Townsley, L. K. et al., 2001b, AJ 122, 1

[Bruzual and Charlot 1993] Bruzual, G. A. & Charlot, S., 1993, ApJ 405, 538

[Calzetti 1997] Calzetti, D., 1997, AJ, 113, 162

[Calzetti et al. 2000] Calzetti, D., Armus, L., Bohlin, R. C., Kinney, A. L., Koornneef, J., & Storchi-Bergmann, T., 2000, ApJ, 533, 682

[Casertano et al. 2000] Casertano, S., de Mello, D., Dickinson, M., Ferguson, H. C., Fruchter, A. S., Gonzalez-Lopezlira, R. A., Heyer, I., et al., 2000, AJ, 120, 2747

[Castelli and Kurucz 1994] Castelli F., & Kurucz R. L., 1994 A&A, 281, 817

[Cohen et al. 1996] Cohen, J. G., Hogg, D. W., Pahre, M. A., & Blandford, R., 1996, ApJ 462, L9

[Cohen et al. 1999a] Cohen, J. G., Hogg, D. W., Pahre, M. A., Blandford, R., Shopbell, P. L., & Richberg, K., 1999, ApJS 120, 171

[Cohen et al. 1999b] Cohen, J. G., Blandford, R., Hogg, D. W., Pahre, M. A., & Shopbell, P. L., 1999, ApJ 512, 30

[Cohen et al. 2000] Cohen, J. G., Hogg, D. W., Blandford, R., Cowie, L. L., Hu, E., Songaila, A., Shopbell, P., & Richberg, K., 2000, ApJ, 538, 29

[Connolly et al. 1997] Connolly, A. J., Szalay, A. S., Dickinson, M., Subbarao, M. U., & Brunner, R. J., 1997, ApJ, 486, L11

[Coleman et al. 1980] Coleman, G. D., Wu, Chi-Chao, & Weedman, D. W., 1980, ApJS, 43, 393

[Dawson et al. 2001] Dawson, S., Stern, D., Bunker, A. J., Spinrad, H., & Dey, A., 2001, AJ, 122, 598

[Dawson et al. 2002] Dawson, S., Spinrad, H., Stern, D., Dey, A., Breugel, W. V., De Vries, W., & Reuland, M., 2002, ApJ, 570, 92

[Dey et al. 1998] Dey, A., Spinrad, H., Stern, D., Graham, J. R., & Chaffee, F. H., 1998, ApJ, 498, L93

[Dickinson 2000] Dickinson, M., 2000, Philosophical Transactions of the Royal Society of London, Series A, Vol. 358, no. 1772, p.2001 (astro-ph/0004028)

[Dickinson et al. 2002] Dickinson M., Giavalisco M., and the GOODS team, in the proceeding of the ESO USM workshop: The Mass of Galaxies at Low and High Redshift, R. Bender and A. Renzini eds. (astro-ph/0204213)

[Ellis et al. 2001] Ellis, R., Santos, M. R., Kneib, J-P, Kuijken, K., 2001, ApJ, 560, L119

[Fan et al. 2001] Fan, X., Strauss, M. A., Schneider, D. P., Gunn, J. E., Lupton, H., Becker, R. H., Davis, M., Newman, J. A. et al., 2001, AJ, 121, 54

[Ferguson et al. 2002] Ferguson, H. C., Dickinson, M., & Papovich, C. 2002, ApJ, 569, L65

[Fernández-Soto et al. 1999] Fernández-Soto, A., Lanzetta, K. M., & Yahil, A., 1999, ApJ, 513, 34

[Fioc and Rocca-Volmerange(1997] Fioc, M., & Rocca-Volmerange, B., 1997, A&A 326, 950

[Giallongo et al. 2002] Giallongo, E., Cristiani, S., D'Odorico, S., & Fontana, A., 2002, ApJ, 568, L9

[Giavalisco et al. 1996] Giavalisco, M., Steidel, C. C., Macchetto, F. D., 1996 ApJ, 470, 189

[Giavalisco et al. 1998] Giavalisco, M., Steidel, C. C., Adelberger, K. L., Dickinson, M., Pettini M., & Kellogg, M., 1998, ApJ, 503, 543

[Giavalisco and Dickinson 2001] Giavalisco, M. & Dickinson, M., 2001, ApJ, 550, 177

[Hogg et al. 2000] Hogg, D. W., Cohen, J. G., & Blandford, R., 2000, ApJ 545, 32

[Irwin et al. 1994] Irwin M., Maddox S., & McMahon R., 1994, Spectrum, 2, 14

[Kodama and Arimoto 1997] Kodama, T., & Arimoto, N., 1997, A & A, 320, 41

[Labbé et al. 2002] Labbé, I., Franx, M., Rudnick, G., Schreiber, N. M. F., Rix, H., Moorwood, A., Van Dokkum P. G., Van Der Werf, P., et al., 2002, preprint (astro-ph/0212236)

[Landolt 1992] Landolt, A.U., 1992, AJ, 104, 340

[Lanzetta et al. 2002] Lanzetta, K. M., Yahata, N., Pascarelle, S., Chen, H-W., & Fernández-Soto, A., 2002, ApJ, 570, 492

[Lilly et al. 1996] Lilly, S. J., Le Fevre, O., Hammer, F., & Crampton, D., 1996, ApJ, 460, L1

[Madau 1995] Madau, P., 1995, ApJ, 441, 18

[Madau et al. 1996] Madau, P., Ferguson, H. C., Dickinson, M. E., Giavalisco, M., Steidel, C. C., & Fruchter, A., 1996, MNRAS, 283, 1388

[Madau et al. 1998] Madau, P., Pozetti, L., & Dickinson, M., 1998, ApJ, 498, 106

[Madau et al. 1999] Madau, P., Haardt, F., & Rees, M. J., 1999, ApJ, 514, 648

[Meurer et al. 1999] Meurer, G. R., Heckman, T. M., & Calzetti, D. 1999, ApJ, 521, 64

[Miyazaki et al. 1998] Miyazaki, S., Sekiguchi, M., Imi, K., Okada, N., Nakata, F., & Komiyama, Y., 1998, Optical Astronomical Instrumentation (Proc. SPIE 3355), S. D'Odorico ed., 363

[Miyazaki et al. 2002] Miyazaki, S., Komiyama Y., Sekiguchi, M., Okamura S., Doi, M., Furusawa, H., Hamabe, M., Imi, K. et al., 2002, PASJ, 54, 833

[Mo and Fukugita 1996] Mo, H. J., & Fukugita, M., 1996 ApJ, 467, L9

[Monet et al. 1998] Monet, D., Bird, A., Canzian, B., Dahn, C., Guetter, H., Harris, H., Henden, A., Levine, S. et al., 1998, The USNO-A2.0 Catalogue, (U.S. Naval Observatory, Washington DC).

[Nagamine et al. 2001] Nagamine, K., Fukugita, M., Cen, R., & Ostriker, J. P., 2001, ApJ, 558, 497

[Nagamine 2002] Nagamine, K., 2002, ApJ, 564, 73

[Nandra et al. 2002] Nandra, K., Mushotzky, R. F., Arnaud, K., Steidel, C. C., Adelberger, K. L., Gardner, J. P., Teplitz, H. I., & Windhorst, R. A., 2002, ApJ 576, 625

[Ouchi et al. 1999] Ouchi, M., Yamada, T., Kawai, H., & Ohta, K., 1999, ApJ, 517, L19

[Ouchi et al. 2001a] Ouchi, M., Shimasaku, K., Okamura, S., Doi, M., Furusawa, H., Hamabe, M., Kimura, M., Komiyama, Y. et al., 2001, ApJ, 558, L83

[Ouchi et al. 2002] Ouchi, M., Shimasaku, K., Okamura, S., Doi, M., Furusawa, H., Hamabe, M., Kimura, M., Komiyama, Y. et al., 2002, the proceedings of the Marseille 2001 conference "Where is the Matter? Tracing Dark and Bright Matter with the New Generation of Large-Scale Surveys" (astro-ph/0109252)

[Papovich et al. 2001] Papovich, C., Dickinson, M., & Ferguson, H. C., 2001, ApJ, 559, 620

[Pascarelle et al. 1998] Pascarelle, S. M., Lanzetta, K. M., & Fernández-Soto, A., 1998, ApJ, 508, L1

[Pettini et al. 2001] Pettini, M., Shapley, A. E., Steidel, C. C., Cuby, J.-G., Dickinson, M., Moorwood, A. F. M., Adelberger, K. L., & Giavalisco, M., 2001, ApJ, 554, 981

[Pickles 1998] Pickles, A.J., 1998, PASP, 110, 863

[Sawicki and Yee(1998] Sawicki, M. & Yee, H. K. C., 1998, AJ, 115, 1329

[Seibert et al. 2002] Seibert, M., Heckman, T. M., Meurer, G. R., 2002, AJ 124, 46

[Shapley et al. 2001] Shapley, A. E., Steidel, C. C., Adelberger, K. L., Dickinson, M., Giavalisco, M., & Pettini, M., 2001, ApJ, 562, 95

[Smail et al. 1997] Smail, I., Ivison, R. J., Blain, A. W., 1997, ApJ 490, L5

[Smail et al. 2002] Smail, I., Ivison, R. J. Blain, A. W., Kneib, J.-P., 2002, MNRAS 331, 495

[Somerville et al. 2001] Somerville, R. S., Primack, J. R., & Faber, S. M., 2001, MNRAS, 320, 504

[Spinrad et al. 1998] Spinrad, H., Stern, D., Bunker, A., Dey, A., Lanzetta, K., Yahil, A., Pascarelle, S., & Fernández-Soto, A., 1998, AJ, 116, 2617

[Springel and Hernquist 2002] Springel, V., & Hernquist, L., 2002, submitted to MNRAS (astro-ph/0206395)

[Steidel and Hamilton 1992] Steidel, C. C., & Hamilton, D., 1992, AJ, 104, 941

[Steidel and Hamilton 1993] Steidel, C. C., & Hamilton, D., 1993, AJ, 105, 2017

[Steidel et al. 1995] Steidel, C. C., Pettini, M. Hamilton, D., 1995, AJ 110, 2519

[Steidel et al. 1996a] Steidel, C. C., Giavalisco, M., Dickinson, M., & Adelberger, K. L., 1996a, AJ, 112, 352

[Steidel et al. 1996b] Steidel, C. C., Giavalisco, M., Pettini, M., Dickinson, M., & Adelberger, K. L., 1996b, ApJ, 462, L17

[Steidel et al. 1998] Steidel, C. C., Adelberger, K. L., Dickinson, M., Giavalisco, M., Pettini, M., & Kellogg, M., 1998, ApJ, 492, 428

[Steidel et al. 1999] Steidel, C. C., Adelberger, K. L., Giavalisco, M., Dickinson, M., & Pettini, M., 1999, ApJ, 519, 1

[Steidel et al. 2001] Steidel, C. C., Pettini, M., & Adelberger, K. L., 2001, ApJ, 546, 665

[Stern and Spinrad 1999] Stern, D. & Spinrad, H., 1999, PASP, 111, 1475

[Sullivan et al. 2000] Sullivan, M., Treyer, M. A., Ellis, R. S., Bridge, T. J., Milliard, B., & Donas J., 2000, MNRAS 312, 442

[Teplitz et al. 2000] Teplitz, H. I., Malkan, M. A., Steidel, C. C., McLean, I. S., Becklin, E. E., Figer, D. F., Gilbert, A. M., Graham, J. R. et al., 2000, ApJ, 542, 18

[Tresse et al. 2002] Tresse L., Maddox S. J., Le Fèvre O., & Cuby J. -G., 2002, MNRAS, 337, 369

[Tyson(1988] Tyson, J. A., 1988, AJ, 96, 1

[Webb et al. 2003] Webb, T. M., Eales, S., Foucaud, S., Lilly, S. J., McCracken, H., Adelberger, K., Steidel, C. et al., 2003, ApJ 582, 6

[Weymann et al. 1998] Weymann, R. J., Stern, D., Bunker, A., Spinrad, H., Chaffee, F. H., Thompson, R. I., & Storrie-Lombardi, L. J. 1998, ApJ, 505, L95

[Williams et al. 1996] Williams, R. E., Blacker, B., Dickinson, M., Dixon, W. V. D., Ferguson, H. C., Fruchter, A. S., Giavalisco, M., Gilliland, R. L. et al., 1996, AJ, 112, 1335